STRUCTURAL CHARACTERIZATION OF MICROMECHANICAL PROPERTIES IN ASPHALT USING ATOMIC FORCE MICROSCOPY

A Thesis

by

ROBERT GROVER ALLEN

Submitted to the Office of Graduate Studies of
Texas A&M University
in partial fulfillment of the requirements for the degree of

MASTER OF SCIENCE

December 2010

Major Subject: Civil Engineering

STRUCTURAL CHARACTERIZATION OF MICROMECHANICAL PROPERTIES IN ASPHALT USING ATOMIC FORCE MICROSCOPY

A Thesis

by

ROBERT GROVER ALLEN

Submitted to the Office of Graduate Studies of
Texas A&M University
in partial fulfillment of the requirements for the degree of

MASTER OF SCIENCE

Approved by:

Chair of Committee,	Dallas N. Little
Committee Members,	Amy L. Epps Martin
	Charles J. Glover
Head of Department,	John Niedzwecki

December 2010

Major Subject: Civil Engineering

ABSTRACT

Structural Characterization of Micromechanical Properties in Asphalt Using Atomic Force Microscopy. (December 2010)
Robert Grover Allen, B.S., Louisiana Tech University
Chair of Advisory Committee: Dr. Dallas N. Little

The purpose of this study was to characterize the micromechanical properties of various structural components in asphalt using Atomic Force Microscopy (AFM). The focus of the study was based on nano-indentation experiments performed within a micro-grid of asphalt phases in order to determine micromechanical properties such as stiffness, adhesion and elastic/plastic behavior. The change in microstructure and micromechanical behavior due to oxidative aging of the asphalt was also a primary focus of the study. The experiment was performed with careful consideration of AFM artifacts, which can occur due to factors such as geometry of the cantilever tip, hysteresis, filtering methods and acoustic vibrations. The materials used in this study included asphalts AAB, AAD and ABD from the Materials Reference Library (MRL) of the Strategic Highway Research Program (SHRP), chosen due to variations in crude source, chemical composition and elemental analysis for each asphalt type.

The analysis of nano-indentation creep measurements corresponding to phase-separated regions ultimately revealed heterogeneous domains in asphalt with different mechanical properties, and oxidative aging was found to induce substantial microstructural change within these domains, including variations in phase structure, phase properties and phase distribution. The form and extent of these changes, however, were different for each asphalt studied. Data analysis and information collected during this study were used for comparisons to existing models and asphalt data, which validated results and established correlations to earlier, related studies. From these comparisons, it was found that data parallels followed expected trends; furthermore, analogous interpretations and distinctions were made between results from this study and the micellar and microstructural models of asphalt. This study of micromechanical properties that govern asphalt behavior has yielded information essential to the advancement of hot mix asphalt (HMA) performance, including a new asphalt "weak zone" hypothesis and a foundation of data for implementation into new and existing asphalt models.

TABLE OF CONTENTS

TABLE OF CONTENTS (CONTINUED)

LIST OF FIGURES

LIST OF FIGURES (CONTINUED)

LIST OF FIGURES (CONCLUDED)

LIST OF TABLES

TABLE Page

1. INTRODUCTION

Currently, there is limited understanding of the complex micromechanical behavior of asphalt, and due partially to this fact, the in-service life of hot mix asphalt (HMA) pavements is often difficult to predict. Although asphalt binder typically accounts for less than ten percent of a HMA mixture, the overall performance of HMA is largely due to the mechanical properties of the asphalt binder. It is generally accepted that the spatial distribution of micromechanical structures governs macromechanical behavior in asphalt, but due to varying chemical and structural compositions with crude oil source combined with the complex rheological and thermoplastic behavior of asphalt, it is difficult to fully understand its mechanical behavior. Empirical data and mechanistic approaches provide good indications of pavement performance, but due to the high variability of environmental and loading conditions to which pavements are exposed, there is a growing need to understand how the micromechanical behavior of asphalt influences the overall performance of HMA. Mechanical behavior of microstructural regions in asphalt can influence asphalt properties such as stiffness, elasticity and plasticity, adhesion, surface charge densities and healing. By developing a clearer understanding of the micromechanical behavior of asphalt and linking that behavior to known macromechanical asphalt properties, longer-lasting and better performing pavements can be constructed.

This thesis follows the style and format of *Journal of Materials in Civil Engineering*.

The following sections describe background information, the main problem and research tasks for the topic studied in this thesis.

1.1 BACKGROUND

One of the greatest challenges to understanding and predicting asphalt behavior is due to the high level of variability between different asphalt sources resulting from factors such as asphalt chemical composition and microstructure (Masson et al., 2005); therefore, in order to properly characterize micromechanical properties of asphalt, it is important to have a thorough understanding of the traditional and current methods used to characterize the chemical composition and microstructure of asphalt. Methods of study to determine asphalt molecular composition include gas chromatography, mass spectroscopy, differential scanning calorimetry, and Fourier transform infrared spectroscopy. Approaches such as X-ray diffraction, size-exclusion chromatography (SEC) and various microscopy techniques have been used to study asphalt microstructure, including scanning electron microscopy, transmission electron microscopy, phase contrast microscopy, polarized light microscopy, laser-scanning microscopy, fluorescence microscopy, and atomic force microscopy (AFM). The leading asphalt characterization models that have evolved from using many of these methods are the micellar (historical) model and the microstructural model.

Depending on the mode of operation, AFM can be used to provide insight into surface topography, phase separation and mechanical properties such as adhesion and stiffness. Although AFM has been employed to study biological samples for a few decades, AFM is still a relatively new tool for investigating micromechanical behavior of asphalt. To provide direct information regarding the mechanical properties of various structural regions, AFM can be used in spectroscopy mode (SM) mode to measure the nano-scale indentation response of asphalt. Unlike contact mode (CM) and non-contact mode (NCM), SM mode is a non-imaging mode in which the tip is moved vertically with respect to the sample surface. The combined use of different AFM operational modes and various experimental conditions provides the basis for a comprehensive examination of asphalt micromechanical properties; however, meaningful data and results can only be obtained from AFM experiments through careful review of necessary background knowledge and the use of vigilant measures to avoid artifacts.

1.2 PROBLEM STATEMENT

Jäger et al. (2004) and Masson et al. (2005) have conclusively shown that as many as four to six different micro-domains with potentially different mechanical properties can exist within an asphalt specimen. As these studies show, utilization of AFM to characterize asphalt microstructure has found the presence of multiple phases and different mechanical properties; however, many questions remain regarding these mechanical properties and how they are affected by factors such as temperature, aging, and binder dissolution in solvents. A specific concern demonstrated by Costa and Yin (1999) is that estimation of mechanical properties using the AFM requires consideration of indentation depth due to possible binder nonlinearity. Another problem that AFM researchers face is that no direct correlations have been made between asphalt-related

AFM studies and historical asphalt models such as the micellar model and Strategic Highway Research Program (SHRP) microstructural model. Jones and Kennedy (1992) proposed that the microstrucural model, developed in the 1980s, made the earlier micellar model obsolete; however, as stated by Masson et al. (2007), many modern-day asphalt researchers still reference the micellar model as a valid model for describing asphalt behavior. These discrepancies support the ongoing need for a better understanding of asphalt chemistry and microstructure. The goal of this research is to further understand the link between asphalt chemistry and pavement performance by building on historical models and results obtained from previous AFM studies. This research will provide new and supporting evidence of either a direct or insignificant influence that micromechanical behavior and various external factors have on asphalt performance. The objectives of this research will be met by using AFM to analyze asphalts with varying chemical compositions under a wide variety of experimental conditions.

1.3 RESEARCH METHODOLOGY

This section outlines and summarizes the research tasks performed during this study. These tasks were as follows:

1.3.1 Task 1: Literature Review

The purpose of this step was to gain understanding of related subjects such as asphalt microstructure and chemical composition, in conjunction with techniques, artifacts and asphalt studies associated with AFM. Knowledge of these topics was gained through reviewing available literature and relevant websites.

1.3.2 Task 2: Sample Preparation

In this step, multiple thin-film specimens of different asphalt types were prepared for testing using a spin coating method, which involved complete dissolution of a known weight of asphalt in toluene. A number of these samples were aged in both the rolling thin-film oven (RTFO) and pressure aging vessel (PAV) to evaluate the effects of long-term oxidative aging on the asphalt's microstructure.

1.3.3 Task 3: Trial Testing and Cantilever Tip Calibration

Trial specimens were prepared, studied and tested using AFM equipment while varying the cantilever tip, mode of operation, depth of indentation and asphalt type. This step was necessary to fine-tune the experimental procedure, identify potential artifacts and ensure that accurate and comparable results were obtainable.

1.3.4 Task 4: Experimental Testing and Data Collection

Once trial testing and calibrations were completed, individual specimens were studied and tested using AFM. The preparation and testing of asphalts AAB, AAD and ABD were performed according to the flowchart shown in Figure 1.1.

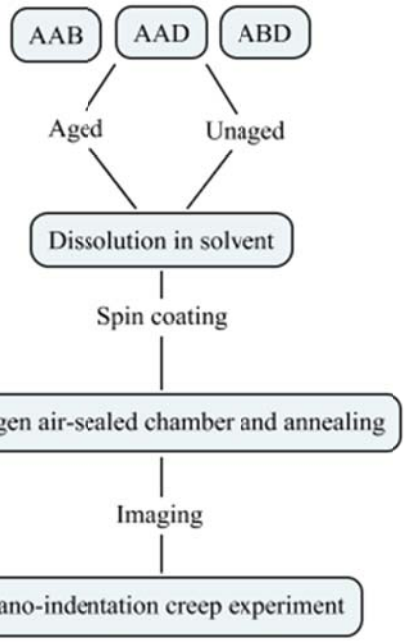

Figure 1.1. Experimental flowchart.

1.3.5 Task 5: Data Analysis and Characterization

In this step, all data measurements were organized and compiled for evaluation and characterization. The analysis included evaluation of topography images, phase detection microscopy (PDM) and SM data for various samples. Finally, an assessment was performed to characterize the microstructural properties and behavior of the asphalts by using statistical analysis and establishing correlations to existing models.

1.4 THESIS OUTLINE

This thesis is organized in five sections as subsequently described. Section 1 presents an introduction that includes background information, problem statement and research methodology. Section 2 presents a literature review of relevant topics. Section

3 outlines the experimental design, including materials and equipment, experimental procedure and trial testing. Section 4 presents experimental results and analysis. Section 5 presents conclusions, recommendations and future work.

2. LITERATURE REVIEW

This section includes a summary of the necessary background information required to meet the objectives and understand the limitations of the experiment. First, traditional methods and models used to describe asphalt chemical composition and microstructure are presented. Next, a description of AFM techniques, modes of operation and related studies are discussed. A review of the limitations and common artifacts associated with AFM is also presented.

2.1 ASPHALT CHEMICAL COMPOSITION AND MICROSTRUCTURE

Asphalt is an extremely complex mixture of hydrocarbons, heteroatoms and metals that combine to form millions of different unique molecules that change with age, temperature and loading conditions. To further complicate the situation, the type and arrangement of these asphalt molecules can vary significantly depending on the crude oil source and manufacturing process. Due to such material complexities, asphalt chemical composition has been the subject of several investigations over the years (Oyekunle, 2006). Several chemical and physical methods have been used to separate asphalt into different chemical groups. As documented by Oyekunle (2006), the historical micellar structural model is based on separation of these fractions into three broad chemical groups composed of poly-nuclear aromatics and hetero-aromatic molecules (asphaltenes), viscous naphtheno-aromatic hydrocarbons (heavy oils) and heterocyclic and polar compounds (resins). The initial relative amount and arrangement of asphaltenes, resins and oils are highly dependent on the crude oil source, and continuous variations in these chemical groups are dependent on temperature, age and loading conditions.

Despite the many advances made through development of the micellar model, historical separation methods were unsuccessful in providing a correlation between chemical composition and physical behavior. In an effort to bridge this gap, a new microstructural model was developed as part of SHRP in the late 1980s. As documented by Jones and Kennedy (1992), this model provided an incomplete, but improved correlation between asphalt chemistry and performance. One of the first chemical separation methods used as the SHRP program evolved was SEC. Effective techniques of SEC were based on the use of toluene as the solvent to minimize disruption of the asphalt structure, while permitting chemical analysis and separation of SEC fractions. As SEC techniques improved over time, the final result was the isolation of two fractions (SEC I and SEC II) from the asphalt. Common terms describing the SEC I fraction are "associated phase" and "polar phase," and collective terms describing the SEC II fraction include "solvent phase" and "non-polar phase." The microstructural model is based on the principle that asphalt is a single-phase, complex mixture of molecules, contrary to the micellar model which exhibited multiple phases of "floating" islands of materials in a "sea" of saturates.

2.2 AFM TECHNIQUES AND ARTIFACTS

AFM was developed by Bennig and coworkers in 1986 (Burnham and Colton, 1989). Since the development of the microstructural model in the late 1980s, there have been many technological advances in microscopy techniques, which have made AFM a very attractive prospect for studying asphalt microstructure. AFM equipment can be used in several different modes of operation, including CM, NCM and SM. The use of different AFM modes can provide valuable insight into the topography, phase separation and mechanical properties of asphalt at the micro-scale. The force applied in NCM is much lower than CM, which is an advantage when studying soft or elastic samples such as asphalt (Raghavan et al., 2000); therefore, NCM was selected as the primary imaging mode for this experiment. Regardless of whether CM or NCM is used for imaging, the same concepts basically apply (Agilent Technologies, Inc., 2007; Burnham et al., 1990; Butt et al., 2005; Winkler et al., 1996), which involves AFM equipment probing the surface of a sample with a sharp tip while interactions between the tip and sample are mapped. The cantilever tip is usually only a couple of microns in length, and this tip is located at the free end of a cantilever with a low spring constant that is 100 to 200 microns in length (Howland and Benatar, 2000). Interatomic (van der Waals) forces between the tip and the sample surface cause the tip to bend or deflect, and this measured deflection allows the computer to generate a map of surface topography. Figure 2.1 shows the effects of van der Waals forces as the tip is moved further away from the sample.

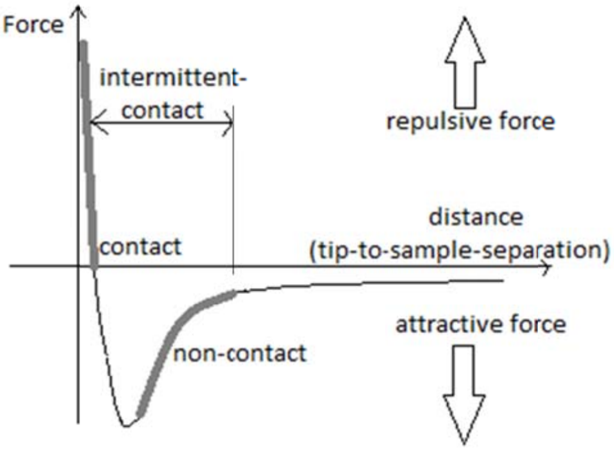

Figure 2.1. Van der Waals forces vs. distance.
(Adapted from Howland and Benatar, 2000)

The AFM detects the position of the cantilever with optical techniques. The most common technique, as shown in Figure 2.2, involves the reflection of a laser beam from the back of the cantilever onto a position-sensitive photo detector (PSPD). As the cantilever bends, due to interactions with the sample surface, the position of the laser beam on the PSPD shifts.

.

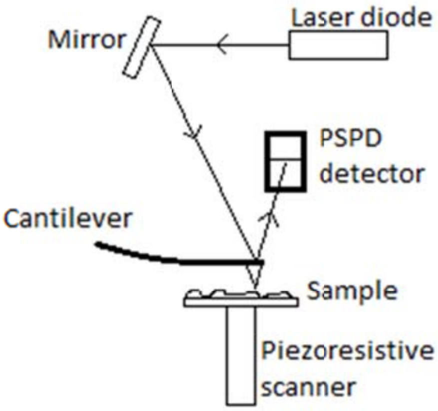

Figure 2.2. Beam-detection deflection scheme.
(Adapted from Howland and Benatar, 2000)

PDM is performed by monitoring the phase lag between two signals: the cantilever oscillation driving signal and the cantilever oscillation output signal. Changes in the phase lag often mean changes in mechanical properties of the sample surface, but additional information is needed to make such an assessment. SM is an extension of the AFM imaging modes that can be used to characterize a sample's mechanical properties. In SM, a constant cantilever deflection is applied vertically into the sample while a periodic signal is applied to the tip. Depending on the mechanical properties of the sample location, a variation in the resulting amplitude of the cantilever modulation results from this signal (Magonov and Reneker, 1997). To fully assess the mechanical properties of the sample, simultaneous comparison involving image topography, PDM images and SM data is required. In addition to these comparisons, the effects of AFM artifacts must also be carefully considered when determining micromechanical properties.

A common problem that engineers and scientists encounter when using measurement instrumentation is artifacts. As documented by West and Starostina (2009), the four primary sources of artifacts in images measured with AFM are probes, scanners, image processing and vibrations. To minimize the likelihood of probe artifacts and ensure accurate dimensional measurements, the probe geometry should be much smaller than the features of the images being measured. Using a probe that is not the optimal size for the application can result in features on a surface appearing too large, features in an image appearing too small, strangely shaped objects or repeating strange patterns in an image. Scanners that move the AFM probe are typically made from piezoelectric ceramics. Self-heating of the piezoelectric ceramics can cause a hysteresis effect and thus introduce artifacts. Scanner artifacts can also be introduced due to geometry of the scanner and positioning of the scanner relative to the sample. To reduce scanner artifacts, precautionary measures should be taken by ensuring perpendicular alignment of the probe and sample, calibrating the scanner, leveling the image and imaging test patterns. Though image processing artifacts are rare, some of the common image artifacts are introduced due to leveling, low pass filtering, smoothing, Fourier filtering and image enhancement. A general rule of thumb to detect image processing artifacts is: "if the image has no noise in it, then the data has likely been compromised (West and Starostina, 2009)." Acoustic and floor vibrations can cause the probe in the microscope to vibrate, resulting in AFM artifacts. Vibration artifacts typically appear as oscillations in the image and can be initiated by something as simple as a person walking by or an airplane flying over a building. As illustrated by Eaton, et al. (2000) and West and Starostina (2009), additional sources of artifacts to consider include sample surface contamination and faulty electronics.

2.3 ASPHALT-RELATED STUDIES USING AFM

This section provides a brief description of some previous experiments involving the use of AFM to study asphalt microstructure. The subsequent three studies described implemented AFM NCM and SM, while varying asphalt types and sample preparation methods to investigate asphalt mechanical properties.

Huang et al. (2005) developed an experimental protocol using AFM to measure surface energies of asphalt on glass plates. Force curves were collected using SM and a thermally-controlled heating stage. The data interpretations were based on the hypothesis that the work of adhesion between asphalt particles and asphalt binders directly relates to the pavement's tendency to microcrack and heal. The theories of the Johnson-Kendell-Roberts (JKR) contact and the Derjaguim-Muller-Toporov (DMT) approach were employed to model air-asphalt film and the asphalt film-glass substrate interfacial system. Several other test methods were also performed as part of the experiment. This paper requires ongoing research to determine the test method that is most predictive of pavement performance in terms of the measurement of adhesive properties between asphalt and the aggregate surface.

Jäger et al. (2004) used AFM NCM and SM to provide insight into surface topography and mechanical properties of two asphalts (B50/70 and B160/220) at room temperature. Randomly distributed "bee-shaped" topography images were observed for both types of asphalt. The "bees" are the result of alternating higher and lower elevations in the surface topography of the asphalt. No correlation was found between the topographic change and alternating asphalts. According to the results, four sub-domains were identified from the surface topography, and each was determined to have different mechanical properties. The reason for the alternating topography of the "bees" was inconclusive, but the "bees" are thought to belong to string-like structures emerging from and immersing at the asphalt surface.

Masson et al. (2005) reported the observation of 13 bulk specimen asphalts prepared by heat-casting, in an effort to maintain the solid-state structure that governs rheology. Topographic and phase-lag images were acquired in NCM at room temperature and at several locations on the sample surface. These results revealed previously seen “bee structures” and previously unseen morphologies with asphalts classified in three groups. One group showed a fine dispersion (0.1–0.7 μm) in a homogenous matrix. Another group showed domains of about 1 μm, and a third group showed up to four different phases of vastly different sizes, which were referred to as catana, peri, para and sal phases. No correlation was found between the PDM morphology and the colloidal system where the asphaltenes are stabilized by polar aromatics in a sea of naphthene aromatics and saturated compounds. This does not necessarily invalidate the model but suggests that it is possibly too simple and that other chemical and structural parameters must be considered to explain the complexity of asphalt. The study showed a good correspondence between the PDM classification and the size of asphalt compounds, which indicates that morphology and molecular arrangement seem partly governed by the size and shape of molecules.

3. EXPERIMENTAL DESIGN

This section describes the asphalt materials, testing equipment and experimental procedure used to prepare the necessary samples and obtain the required data for this experiment. All asphalt aging was performed in the McNew Materials Testing Laboratory at Texas Transportation Institute (TTI). Asphalt thin-film preparation was performed at the Materials Characterization Facility (MCF), and experimental testing with AFM equipment was performed at the Advanced Characterization of Infrastructure Materials (ACIM) Laboratory at Texas A&M University.

3.1 MATERIALS AND EQUIPMENT

3.1.1 Materials

The different materials used in this study include asphalts AAB, AAD and ABD from SHRP's Materials Reference Library (MRL). These asphalts were selected for their differences in crude source, chemical composition, elemental analysis and viscoelastic properties. Tables 3.1 and 3.2 provide a summary of the chemical and physical properties of these asphalts as documented by Mortazav and Moulthrop (1993). As shown in Table 3.1, asphalts AAB and AAD have similar chemical composition and dissimilar elemental content; whereas, asphalt ABD has dissimilar chemical composition and elemental content than that of asphalts AAB and AAD.

Table 3.1. Properties of Asphalts Studied.

Asphalt	Source/Type	Composition				Elemental Analysis				
		As	PA	NA	S	N(%)	S(%)	V(ppm)	N(ppm)	Fe(ppm)
AAB	Wyoming High Sulfur	19.3	38.3	33.4	8.6	0.5	4.7	220.0	56.0	16.0
AAD	California Coastal	23.9	41.3	25.1	8.6	0.8	6.9	310.0	145.0	13.0
ABD	California Valley	10.2	52.7	28.4	10.4	1.2	1.6	62.0	123.0	54.0

From SHRP MRL: As, asphaltenes; PA, polar aromatics; NA, napthene aromatics; S, saturates

Table 3.2. Classification and Viscoelastic Properties of Asphalts Studied.

Asphalt	Visc./Pen Grade	PG Grade	Original Asphalt		G* (Pa, 60°C, 10 rad/sec)		
			Viscosity (140°F, poise)	Penetration (0.1 mm)	Original	TFOT Aged	PAV Aged
AAB	AC-10	PG58-22	1029	98	2486	3229	8888
AAD	AR-4000	PG58-28	1055	135	3148	3784	11319
ABD	AR-4000	PG58-10	2112	47	NA	6498	NA

From SHRP MRL: TFOT, thin-film oven test; PAV, pressure aging vessel; NA, not available

3.1.2 Equipment

The Agilent 5400 AFM system was used to perform this experiment. The main component of the system is the microscope, which includes the scanner, sample stage, high-resolution probe/tip and detector. In addition to a high-speed computer, the control system must include, at a minimum, an AFM controller and head electronics box (HEB) as presented in Figure 3.1. The AFM controller provides high voltage to the piezo actuators and other control functions, such as closed-loop scanning control. The HEB interprets the signals from the detector and displays the sum signal or the deflection signals. It also provides an oscillating voltage for AC mode imaging.

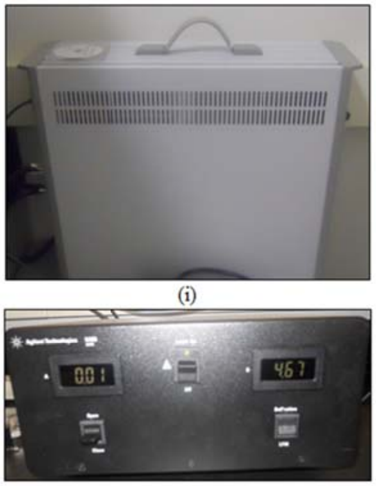

Figure 3.1. (i) AFM controller and (ii) HEB.

The AFM equipment consists of several major components. All AFM imaging and SM force indentation techniques are performed by using a tip mounted to the free end of a cantilever probe, which is fabricated from silicon or silicon nitride. The cantilever is mounted onto the nose assembly, which retains and secures the cantilever firmly in the scanner module. The cantilevers used for the experiment were PPP-NCL cantilevers, which were manufactured by Nanosensors. These cantilevers have an average resonant frequency of 175 kHz and a force constant ranging from 21-98 N/m. The cantilever tip is conical in shape, which is well-suited for imaging but introduces more variability for force measurements. To process an image, the cantilever rests on the scanner module, moving in a raster motion across a stationary sample. This motion is driven by applying high voltages to the scanner module's piezo elements. Figure 3.2 depicts the typical setup process of mounting a cantilever onto the nose assembly of the scanner module and attaching the scanner to the microscope. Additional components of the microscope including the video system, microscope base, PSPD, and sample area are also identified in Figure 3.2.

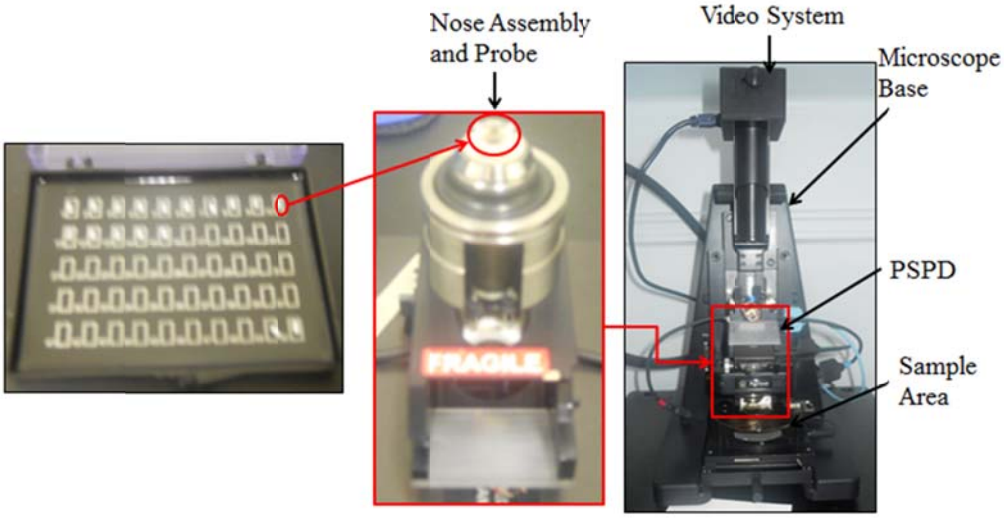

Figure 3.2. Cantilevers, scanner module and microscope.

In addition to the basic AFM functional equipment, optional equipment is often necessary, depending on the environment, to appropriately use AFM. An environmental enclosure and vibration isolation stage, as depicted in Figure 3.3, is required to control vibrations, air turbulence and acoustic noise. Without the aid of these devices, obtaining consistently worthwhile topography and phase images would be extremely difficult. To properly utilize the isolation stage, the vertical position indicator and vertical stiffness adjustments should be used, and the environmental enclosure door should always be secured prior to imaging.

Figure 3.3. AFM environmental enclosure and floating vibration isolation stage.

All aspects of the AFM, including alignment, calibration and imaging are controlled by a software package called PicoView. PicoView also contains an image and data manipulation software tool, which enables the user to study and analyze data that is collected with the AFM. General familiarity with PicoView, as well as the equipment previously described, is requisite to operating the AFM and performing the necessary steps required in this experiment. The AFM work station that was used to conduct this research is shown in Figure 3.4.

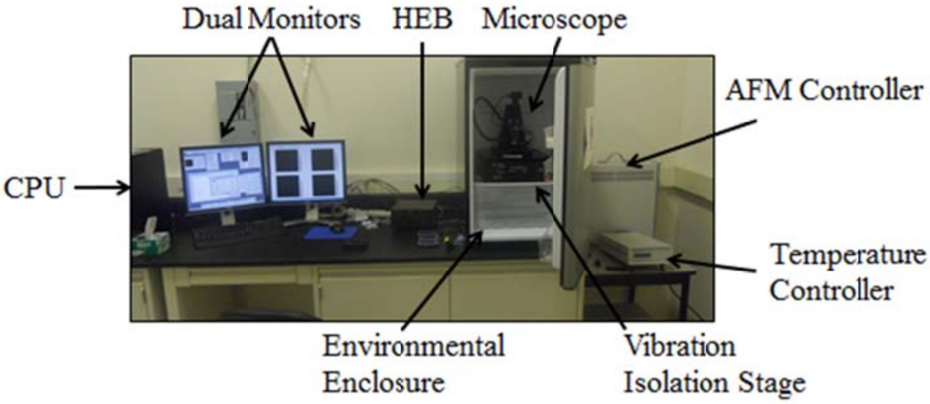

Figure 3.4. AFM work station.

3.2 EXPERIMENTAL PROCEDURE

3.2.1 Sample Preparation

Asphalts AAB, AAD and ABD were aged using both the RTFO procedure according to AASHTO T 240/ASTM D 2872 and the PAV procedure according to AASHTO R 28 to simulate long-term aged asphalt for physical and chemical property testing. The aged specimens were then heated to flowability and placed into cylindrical storage containers for further preparation along with original (unaged) asphalts AAB, AAD and ABD, as shown in Figure 3.5.

Figure 3.5. Original and aged asphalts AAB, AAD and ABD.

After the asphalts were properly prepared and stored, each was then cast into thin films using a conventional solution casting method. Each blend was dissolved by adding 11 mL of high performance liquid chromatography (HPLC) grade toluene per 1.5 g of asphalt. The mixture was prepared approximately 12 hours prior to casting to ensure that the solvent dissolved all of the asphalt. A Laurell WS-650S spin processor, shown in Figure 3.6, was used to cast the thin films. The spin processor was equipped with a 1.75-inch vacuum chuck to properly hold the substrate and prevent leakage into the vacuum prior to starting the motor. Each microscope slide was pre-cleaned with methanol and dried with nitrogen prior to asphalt solution application.

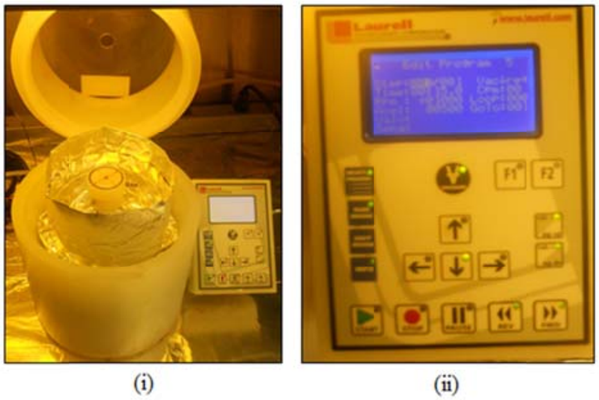
(i) (ii)

Figure 3.6. (i) Laurell WS-650S spin processor and (ii) controller.

A cylinder of aluminum foil was prepared for cleaning purposes, and the glass slide was placed on top of the vacuum chuck to completely cover the O-ring prior to application of the vacuum. After applying the vacuum, spacing between the aluminum foil cylinder and glass slide was checked to ensure adequate coverage for spinning. The spin processor controller was then used to adjust the rotation speed to 1000 rpm for 15 seconds. After adjusting the controller setting, the asphalt solution was applied liberally to the glass slide using a dropper pipet to ensure complete coverage by the asphalt solution. Once the glass slide was completely covered, the motor was started. After spinning for the allotted amount of time (15 seconds), the preparation was complete and the vacuum was removed. This process was repeated for each asphalt. The prescribed method of preparation and casting yields an asphalt film thickness of approximately

1000 ± 200 nm, which is an adequate film thickness for this experiment. An illustration of the spin coating process is shown in Figure 3.7.

To eliminate residual solvent that was used to prepare the thin-film binder specimens, ultra high purity dry nitrogen was passed through a super-clean purifier and into an air-tight heated vacuum desiccator where the thin-film specimens were stored after spin coating. The nitrogen purge was sustained for a minimum of two hours prior to annealing the films for one hour at 50°C to eliminate micro capillaries in the film that may have been created due to the vaporization of toluene under nitrogen purge. An illustration of this process is shown in Figure 3.8.

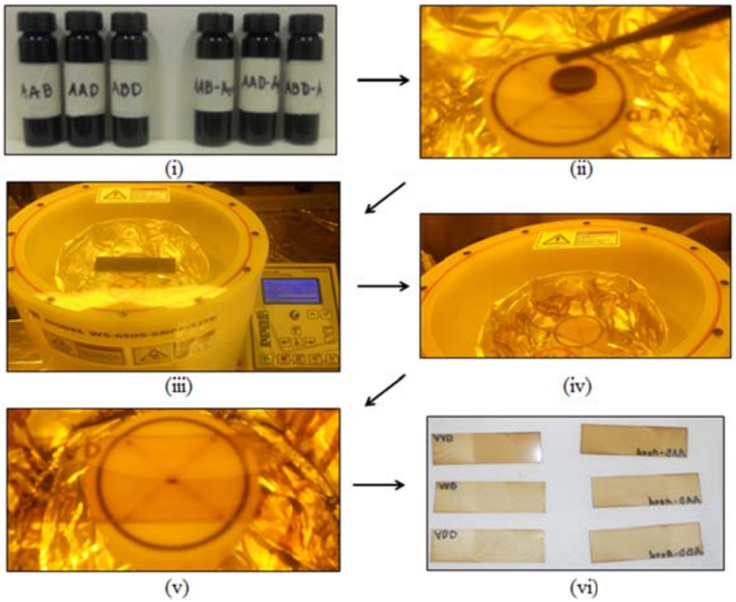

Figure 3.7. (i) asphalt solution for original and aged asphalts AAB, AAD and ABD (ii) application of solution onto clean glass slide (iii) covered glass slide in sealed chamber (iv) casting (v) releasing vacuum seal after casting (vi) thin-film asphalt specimens.

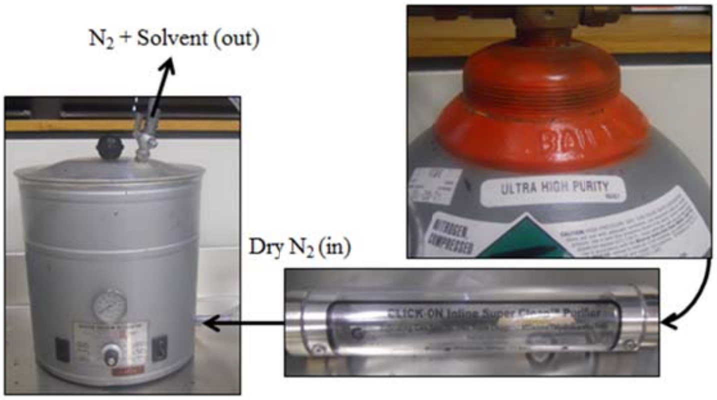

Figure 3.8. Dry nitrogen purge and annealing process.

Due to the thinness of each asphalt film, oxidation can occur very quickly. To prevent rapid oxidation from occurring, each individual thin-film was stored in an air-tight chamber until just prior to imaging and testing with the AFM. Trial testing has shown that omitting this step can result in similar and indistinguishable results for original and aged asphalt of the same type.

3.2.2 Cantilever Tip Calibration and Trial Testing

The probe and tip geometry, cantilever spring constant and cantilever resonant frequencies can vary significantly from cantilever to cantilever, which can cause problems for gathering analogous data during AFM experiments. These variations, in addition to irrepressible changes in manual cantilever alignments, were tested to determine the sensitivity of these parameters in the event that the same probe could not be used throughout the entire experiment. Maintaining a useable probe that has been calibrated presents challenges during testing, because probes can be damaged or contaminated while performing force experiments on stiff materials and while utilizing with sticky materials, such as asphalt.

To determine the consequence of changing cantilevers and/or alignments, the deflection sensitivity of multiple cantilevers was measured. This was performed by allowing the probe to interact with a hard surface, such as a clean glass slide or silicon, while a constant force was applied. The slope of the corresponding force versus distance curve yielded the deflection sensitivity of the cantilever.

The other basic cantilever property that is needed prior to making analogous data comparisons is the cantilever spring constant. There have been several methods offered in the literature for determining the cantilever spring constant, but most of the methods present shortcomings or potential errors themselves. Of the available methods prescribed in the literature, the *thermal k* method was chosen and used to determine the cantilever spring constant for this experiment. This method was successful in generating force constant values that were consistent; however, the values obtained were outside of the expected range of force constant for the given cantilever, and thus could not be used. In order to bypass this issue and proceed with the experiment, a force constant within the expected range of the cantilever was assumed. The *thermal k*-generated force constant was still documented, however, to establish a method for making reasonable comparisons to force measurements collected with other cantilever tips. By documenting the *thermal k*-generated force constants, future correlations could be made based on the relationship between the *thermal k*-generated value and the assumed value.

After evaluating the cantilever sensitivity, trial testing was necessary to fine-tune the experimental procedure, identify potential artifacts and ensure that accurate and comparable results could be obtained throughout the experiment. The entire experiment would require roughly 120-240 force measurements for six asphalts (three aged and three unaged), depending on the number of phases identified using PDM. The primary objective of the trial run was to observe any type of systematic change in data during the progression of data collection. The trial experiment was performed using two separate methods to effectively identify a systematic shift in data:

1. Identify different phases in an asphalt specimen and perform a force measurement in each of the different phases, then repeat a force experiment in the **same** location of each phase. Note any systematic shift.
2. Identify different phases in an asphalt specimen and perform a force measurement in each of the different phases, then repeat a force experiment in a **different** location of each phase. Note any systematic shift.

The trial test consisted of precisely three force measurements taken in each PDM-identified phase. An illustration of the PDM-identified asphalt phases and locations of each measurement for the two trial experiments is shown in Figure 3.9.

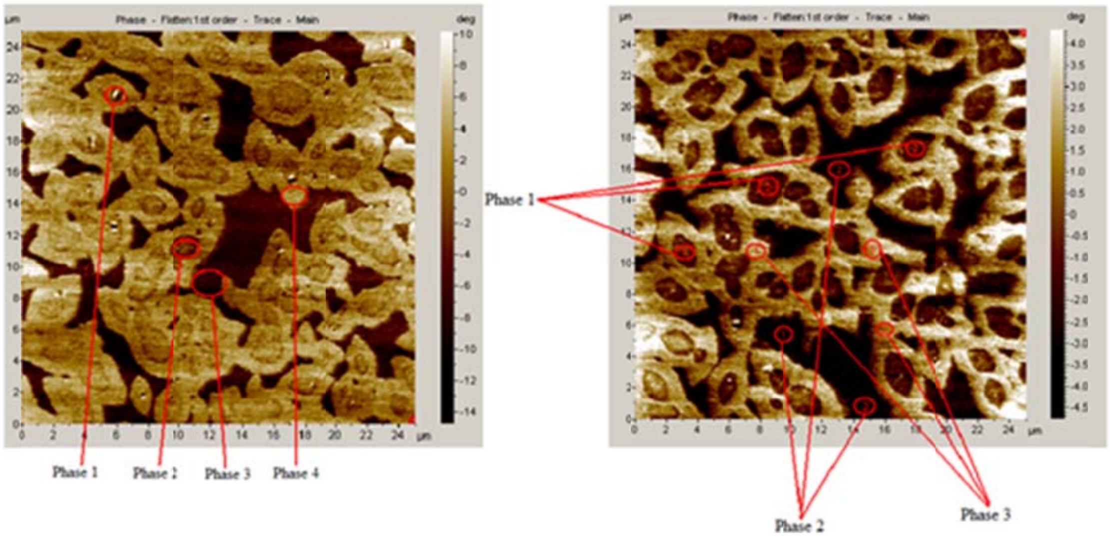

Figure 3.9. Location of force measurements for two trial experiment methods.

To perform each force measurement, the position of the piezo is fixed at a slightly more negative position in the z-direction than the setpoint value. This positioning causes the piezo to lower the tip vertically, which generates a force required for the tip to penetrate the material to the fixed position. After each force measurement was completed, the tip was completely disengaged to a point 20 microns above the sample to ensure that the next measurement was not taken in the same location of the sample. This process was repeated for each measurement. Force measurements were collected such that no consecutive measurements were taken in the same phase; in other words, measurements were taken in the following sequence: phase 1-test 1, phase 2-test 1, phase 3-test 1, phase 4-test 1, phase 1-test 2, etc. This sequence was used to eliminate any data trends specific to an individual phase and also to allow additional measurements to be taken between each individual phase measurement. Using these methods would provide a better indication of the validity of force measurements to be expected throughout the experiment.

3.2.3 PDM Imaging, Experimental Testing and Data Collection

Once calibrations and trial testing were completed, individual specimens were imaged and tested with the AFM. Prior to imaging and testing, several initial steps were required before the AFM was operational. These steps included complete assembly of the scanner into one unit and installation of the scanner into the microscope. Once the scanner was in place, the scanner's laser spot was aligned to reflect off the cantilever. Next, the PSPD was connected to the microscope, and the position of the laser spot on the PSPD was adjusted by observing the deflection, friction and sum values in PicoView. The sample was then mounted onto the sample stage and the cantilever was tuned to its resonant frequency. Finally, by lowering the cantilever into a position in which the setpoint equaled 95 percent of the amplitude, the AFM was operational for imaging.

Obtaining quality topography and phase images proved to be somewhat of an art. After starting the imaging process, the drive percent (amplitude), I-gain, P-gain and setpoint values were manually adjusted until quality real-time images were obtained. This process can take several minutes, depending on the extent of vibrations and acoustic noise present in the laboratory during imaging. All topography and PDM images were obtained in AC mode during this experiment.

After a quality PDM image was obtained, the image remained visible on one of the dual screens, while the mode of operation was changed to SM to perform the force measurements. By simultaneously displaying the phase image and engaging SM, it was possible to use a pointer to direct the force experiment to a specific location of the phase image. A fundamentally different force measurement was, however, performed during the experimental testing than during trial testing. Although force versus distance measurements are useful and convenient for calibration and trial purposes, a more representative measurement was needed to adequately assess the time-dependent behavior of asphalt. Such an assessment was attained by designing a creep test using the custom SM of the AFM. Several potential force applications and load times were examined during trials and prior to selection of the final settings for the creep test. The final creep test settings were designed to bring the tip into contact with a pre-determined location of the sample and apply a constant force of 0.20 V for 4 seconds, while the deflection (change in topography) versus time was measured. After applying the force, it was then removed and the recovery of the material was measured. It was later determined that due to piezo creep and thermal drift issues common to the AFM, it was not possible to consistently measure the recovery of the material after removing the force; therefore, only the material deflection with time was measured during the experiment. All creep measurements were performed using closed-loop scanning, which include high-precision inductive positioning sensors to improve the accuracy of the vertical cantilever positioning and movement.

The same methodology of collecting force measurements during trial testing was applied for the creep measurements, i.e. no consecutive measurements were taken in the same phase. The number of measurements collected during trial testing, however, was increased from three to ten measurements per phase to provide a more representative mean and a more comprehensive indication of data variance. A slightly different process was also required to obtain creep measurements rather than standard force measurements as described subsequently.

To begin a creep test, the tip was slowly brought into contact with the sample surface in contact mode by observing the raw deflection of the cantilever. Immediately after the cantilever tip was in contact with the surface, the test was initiated. After the test was completed, the tip was disengaged from the sample by ejecting the scanner to a point 20 microns above the sample. The next measurement was performed by changing the operating mode to AC mode and performing an automatic approach of the scanner. Once the scanner was within proximity of the sample in NC mode, the operating mode was changed to CM and the tip was slowly brought into contact with the surface as previously described. This process was repeated until ten measurements were collected for each phase and again repeated for all specimens.

3.2.4 Data Analysis and Characterization

During this experiment, two types of images were collected using the AFM imaging modes: topography images and phase images. As previously stated, the primary focus of this study involves the observation of different phases detected by PDM and the measured viscoelastic properties associated with those phases; however, the topographic images collected during this study provided additional information and revealed an interesting correlation between topography and phase change in asphalt. After observing various topography and phase images, it became apparent that topography changes were generally accompanied by phase changes in asphalt. The opposite was not necessarily true; however, as phase changes were not always accompanied by topography changes. The topography images typically indicated differences only when sharp changes in topography were present, such as seen with the characteristic "hills and valleys" amongst "bee" structure phases. Further investigation of the two image types revealed remarkable similarities between topography and phase images whenever "bee" structures were present. From this evidence of image correlation, it seems rational that a phase change in asphalt is also accompanied by a topographic change, even though this relationship is not always apparent in topographic images. This line of reasoning would suggest that the sensitivity of asphalt phase detection is much higher than that of topography detection, or, as indicated by Masson et al. (2005), the limited resolution of optical microscopy is simply not capable of providing details of the structure within the matrix that is provided by PDM. The direct correlation between topography and phase change is illustrated in Figure 3.10.

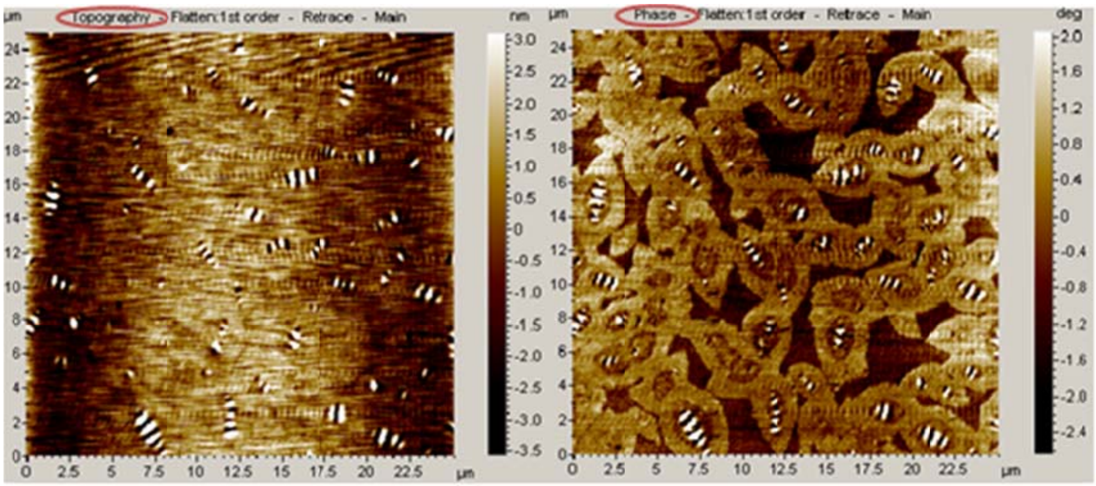

Figure 3.10. Similarities between asphalt topography and phase image.

During the image analysis of each asphalt, profile extractions and three-dimensional images were generated from phase images, based on the correlation between topography and phase change previously described. It should be noted, however, that the three-dimensional topography in each image is enhanced in order to amplify the phase and topography changes on such a small scale; otherwise, typical asphalt topography changes in the range of nanometers would hardly be detectable on a phase image scale of 25 by 25 microns.

To properly characterize the different phases of each asphalt, several commonly reported statistical values were calculated to describe the topography and roughness parameters amongst different phases. The reported values included: root mean squared height (S_q), maximum peak height (S_p), maximum pit height (S_v), maximum height (S_z), arithmetic mean height (S_a), skewness (S_{sk}) and kurtosis (S_{ku}). The S_p, S_v and S_z values were selected to provide valuable information regarding the correlation, if any, between phase changes and major spikes in topography. It is commonly observed that major topography changes occur in the bee structures, and these specific statistical values functioned to verify the extent to which these changes occur, as well as provide insight into possible major topography changes within other phases. S_q is a statistical measure of the degree of variance of the height distribution, which was selected to describe whether the mean surface plane correlates well with the topography of the most dominant asphalt phase or whether significant deviations within individual phases are occurring and thus influencing the location of the mean surface plane. To further explore any trends between topography and phase change, S_{sk} was chosen to describe the extent to which the probability distribution departs from symmetry about its mean height. A resulting negative S_{sk} would indicate that a majority of the height values lie to the right of the mean, and the opposite is true for a positive S_{sk}. A zero S_{sk} would indicate that the height values are relatively evenly distributed on both sides of the mean. To clearly determine the overall flatness of the probability distribution of each asphalt, S_{ku} was calculated. A low S_{ku} describes variance that results from frequent, minor deviations from the mean; whereas, high S_{ku} describes variance that results from occasional, large deviations from the mean. Table 3.3 provides a summary of the values reported.

In addition to using statistical analysis to characterize surface texture, Abbott-Firestone curves were generated for each asphalt to characterize the phase distribution. The Abbott-Firestone curve is mathematically equivalent to the cumulative probability density function of the phase distribution.

Table 3.3. Statistical Values Reported to Describe Roughness Parameters.

Value description	Definition	Value/Equation
Root mean square	Variance of the height distribution	$S_q = \sqrt{\frac{1}{A}\iint z^2(x,y)dxdy}$
Maximum peak height	Height between the highest peak and the mean plane	S_p
Maximum pit height	Depth between the mean plane and the deepest valley	S_v
Maximum height	Height between the deepest valley and the highest peak	S_z
Arithmetic mean	1st moment distribution, describing the mean surface height	$S_a = \sqrt{\int z(x,y)dxdy}$
Skewness	3rd statistical moment, qualifying the symmetry of distribution	$S_{sk} = \frac{1}{{S_q}^3}\sqrt{\frac{1}{A}\iint z^3(x,y)dxdy}$
Kurtosis	4th statistical moment, describing flatness of distribution	$S_{ku} = \frac{1}{{S_q}^4}\sqrt{\frac{1}{A}\iint z^4(x,y)dxdy}$

Adapted from Agilent Technologies, Inc., 2007

After characterizing the topography and morphology of each binder using statistical analysis, a thorough study was performed to analyze the creep data collected using the AFM SM. For this experiment, approximately 250 data points were collected during each four-second creep test, and each creep test was repeated roughly 140 times. To manipulate such a large amount of data, the data files were initially saved in ASCII format and later imported into Microsoft excel for analysis. The data output was originally in the form of relative topography change versus time; however, since relative topography change varies at any given location, absolute topography change, or material deflection, versus time was needed to make useful comparisons between different measurements. Absolute topography change was thus calculated by subtracting initial topography from the topography at each data point. This process was repeated for each data set and compiled for further analysis as shown in Figure 3.11. Once the absolute topography change was calculated for each creep measurement, or sub-phase, individual curves were plotted together for a single phase comparison of variability between measurements. An average material deflection and standard deviation for each phase was then calculated from the ten sub-phases and superimposed onto the same graph with the average deflection of other phases. This allowed for comparison of maximum deflection variances amongst the different phases.

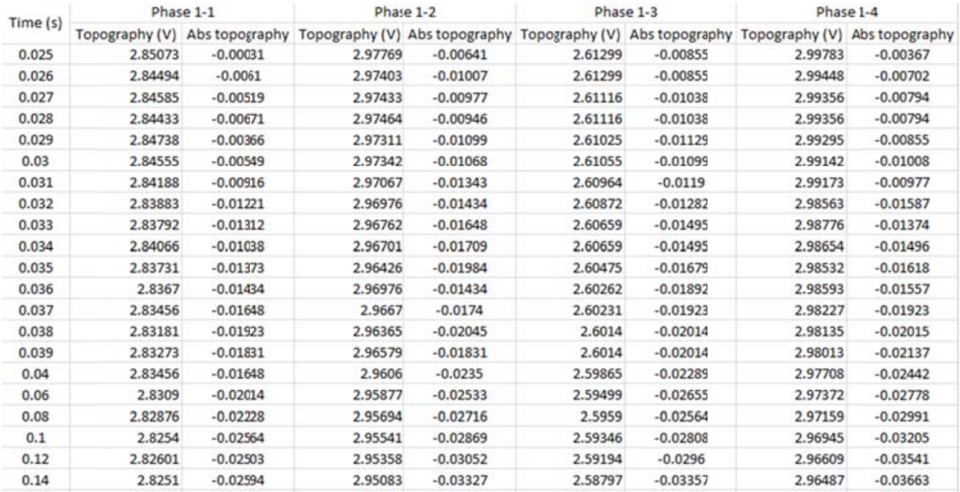

Time (s)	Phase 1-1		Phase 1-2		Phase 1-3		Phase 1-4	
	Topography (V)	Abs topography	Topography (V)	Abs topography	Topography (V)	Abs topography	Topography (V)	Abs topography
0.025	2.85073	-0.00031	2.97769	-0.00641	2.61299	-0.00855	2.99783	-0.00367
0.026	2.84494	-0.0061	2.97403	-0.01007	2.61299	-0.00855	2.99448	-0.00702
0.027	2.84585	-0.00519	2.97433	-0.00977	2.61116	-0.01038	2.99356	-0.00794
0.028	2.84433	-0.00671	2.97464	-0.00946	2.61116	-0.01038	2.99356	-0.00794
0.029	2.84738	-0.00366	2.97311	-0.01099	2.61025	-0.01129	2.99295	-0.00855
0.03	2.84555	-0.00549	2.97342	-0.01068	2.61055	-0.01099	2.99142	-0.01008
0.031	2.84188	-0.00916	2.97067	-0.01343	2.60964	-0.0119	2.99173	-0.00977
0.032	2.83883	-0.01221	2.96976	-0.01434	2.60872	-0.01282	2.98563	-0.01587
0.033	2.83792	-0.01312	2.96762	-0.01648	2.60659	-0.01495	2.98776	-0.01374
0.034	2.84066	-0.01038	2.96701	-0.01709	2.60659	-0.01495	2.98654	-0.01496
0.035	2.83731	-0.01373	2.96426	-0.01984	2.60475	-0.01679	2.98532	-0.01618
0.036	2.8367	-0.01434	2.96976	-0.01434	2.60262	-0.01892	2.98593	-0.01557
0.037	2.83456	-0.01648	2.9667	-0.0174	2.60231	-0.01923	2.98227	-0.01923
0.038	2.83181	-0.01923	2.96365	-0.02045	2.6014	-0.02014	2.98135	-0.02015
0.039	2.83273	-0.01831	2.96579	-0.01831	2.6014	-0.02014	2.98013	-0.02137
0.04	2.83456	-0.01648	2.9606	-0.0235	2.59865	-0.02289	2.97708	-0.02442
0.06	2.8309	-0.02014	2.95877	-0.02533	2.59499	-0.02655	2.97372	-0.02778
0.08	2.82876	-0.02228	2.95694	-0.02716	2.5959	-0.02564	2.97159	-0.02991
0.1	2.8254	-0.02564	2.95541	-0.02869	2.59346	-0.02808	2.96945	-0.03205
0.12	2.82601	-0.02503	2.95358	-0.03052	2.59194	-0.0296	2.96609	-0.03541
0.14	2.8251	-0.02594	2.95083	-0.03327	2.58797	-0.03357	2.96487	-0.03663

Figure 3.11. Screenshot of typical data file containing creep measurements.

The previously described approach of combining phase images, profile extractions, three-dimensional phase depictions, surface texture statistical analysis, graphical phase distribution and extensive creep measurements of all phases provided a comprehensive basis for characterization of each asphalt. Once the data were analyzed, relative comparisons were made between the compiled data and existing models, and the observed microstructural behavior of the PDM-identified asphalt phases was interpreted.

4. RESULTS, DATA ANALYSIS AND CHARACTERIZATION

This section describes the results of calibration and trial testing, followed by the experimental results, analysis and characterization methods. Results feature phase imaging, profile extractions, three-dimensional phase depictions, surface texture statistical analysis, graphical phase distribution and all creep measurements performed during this experiment. The layout of this section includes presentation of results for each individual asphalt, followed by comparisons between different asphalts and the effects of aging on each. The section concludes with comparisons between force measurements collected during this study and data documented in SHRPs MRL.

4.1 CANTILEVER TIP CALIBRATION AND TRIAL TESTING

To properly determine the sensitivity of varying cantilever tips and alignments, three supposed replicate probes and alignments were examined. It was determined that the deflection sensitivity of each cantilever, and thus respective force measurement, varies significantly due to changing or re-alignment, as shown in Figure 4.1. The AFM software, PicoView, allows the user to enter the force constant and the deflection sensitivity (slope of force versus distance calibration curve) of the cantilever tip prior to taking measurements, but due to the high variability and sensitivity of each cantilever, the likelihood of attaining invalid results increases by changing or re-aligning cantilever tips during an experiment.

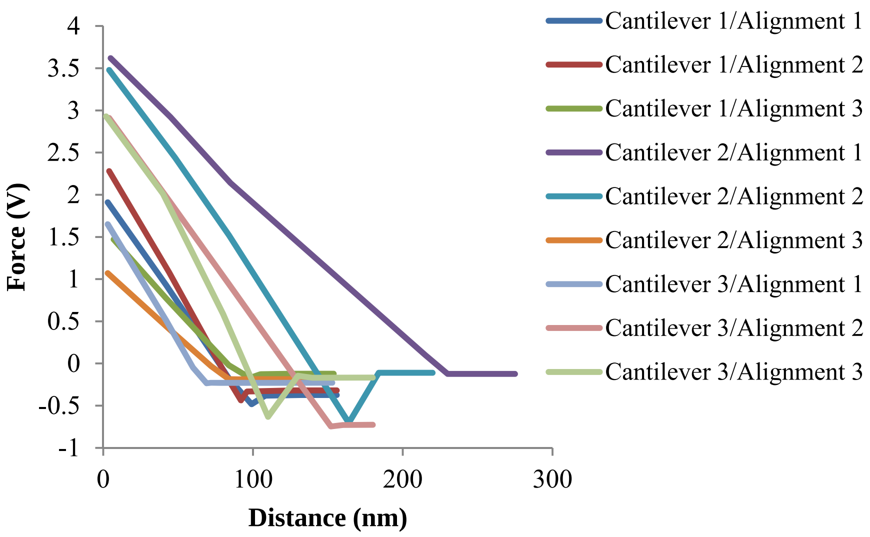

Figure 4.1. Deflection sensitivity for varying cantilevers and alignments.

Due to the cantilever sensitivity findings previously described and the lack of a sound and timely method for accurately measuring the force constant of each cantilever tip, the ability to repeat accurate and consistent measurements with the same cantilever tip became a key focus prior to the experiment. It was revealed through trial testing that accurate and repeatable measurements were obtainable by using a single cantilever during the experiment, as long as the tip remained functional. For asphalt studies involving AFM SM, a key concern with using a single tip for multiple force measurements is the potential for contamination of the cantilever tip by the highly adhesive material. This is especially a concern if the asphalt has been heated prior to testing. It was thus conceived, prior to testing, that material would accumulate on the cantilever tip and result in a systematic change in force measurements as the experiment progressed, but results of the trial experiment alleviated such concerns. As shown in

Figure 4.2, force measurements taken in the **same** location of each phase consistently resulted in a systematic shift upwards in data, which indicated a higher material stiffness with each measurement. As illustrated in Figure 4.3, the next trial of measurements taken at **different** locations within each phase yielded consistent measurements with no apparent systematic shift in data. These findings suggest that the systematic increase observed during the first trial was the result of disturbing or compacting the test location with each progressive measurement and not due to tip contamination or invalid measurements.

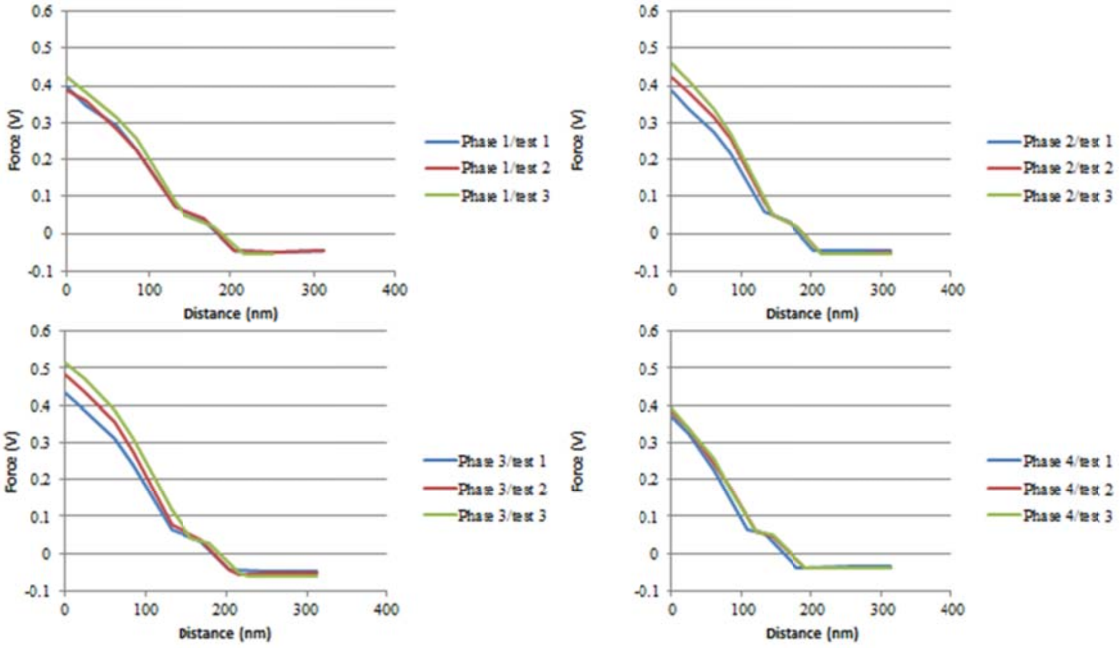

Figure 4.2. Repeating force measurements in the same location of four phases.

While variations in cantilever properties offers significant challenges, failing to acknowledge these effects while collecting force data could result in apparent false changes in stiffness and thus inaccurate force measurements. It was determined that by avoiding data collection in repetitive locations, a single cantilever could confidently be used to collect accurate and consistent force measurements throughout the experiment.

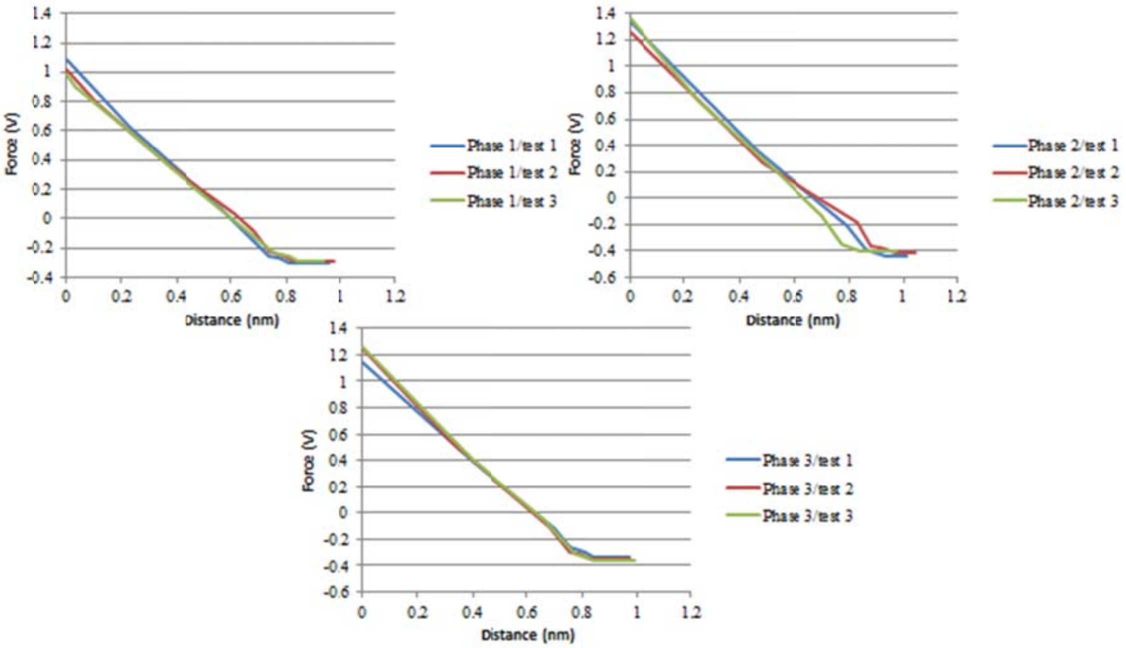

Figure 4.3. Repeating force measurements in different locations of three phases.

4.2 EXPERIMENTAL RESULTS AND ANALYSIS

Based on the findings from the trial experiment, a single cantilever was selected and calibrated for use in PDM mode and SM to perform the experiment. The cantilever used during the experiment had a deflection sensitivity of 59.27 V/nm, an assumed force constant of 41 N/m and a resonant frequency of 169.46 kHz. These values were entered into PicoView prior to performing the SM creep tests. Information regarding the cantilever properties was documented so that supplementary data collected using a different cantilever during other experiments could be used for reasonable comparisons between the two data sets. As previously stated, however, the *thermal k*-determined force constant of 0.011 N/m is also required to make analogous comparisons between data sets.

4.2.1 Asphalt AAB

Figure 4.4 presents a 25 by 25 μm phase image of asphalt AAB. As shown, two distinctive phases were recognized, and the distribution of the two phases was completely random. The phases were identified as Phase 1 and Phase 2; whereas, Phase 1 and Phase 2 appear to be the dispersing phase and the dispersed phase, respectively. The overall size and shape of Phase 2 is rather variable, but the approximate longest dimension ranges from 1 to 6 μm. From the profile extraction, it is apparent that slight variations in topography are present amongst each individual phase, but the boundaries of Phase 2 generally depict gradual increase in topography to a peak value.

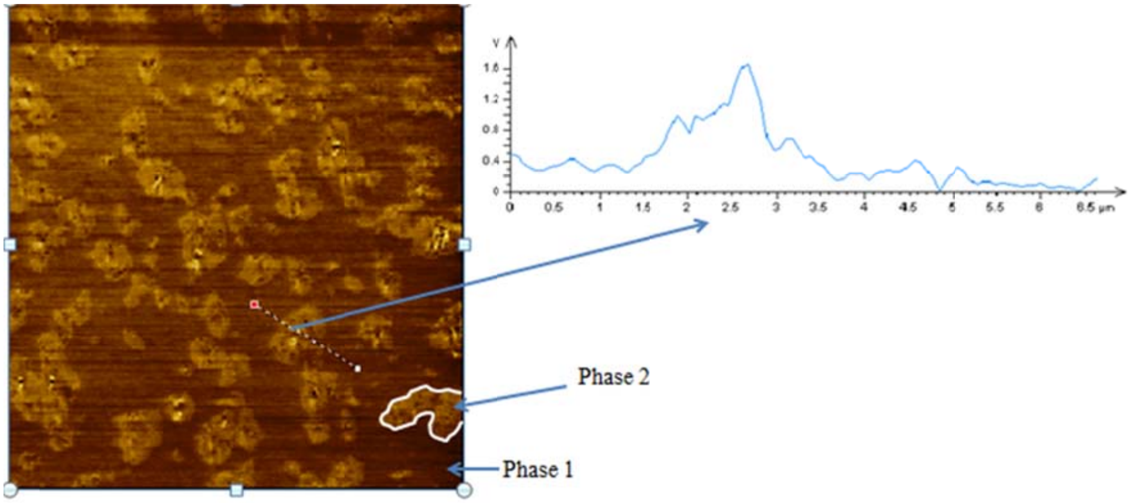

Figure 4.4. Phase image and profile extraction of asphalt AAB.

Figure 4.5 shows a three-dimensional depiction of asphalt AAB, including statistical analysis of surface texture and an Abbott-Firestone curve to describe the distribution of different phases. The statistical analysis indicates that S_p and S_v were 175 nm and 155 nm, respectively. S_z was 330 nm, and S_a of the two distinctive phases was 76.4 nm. S_q was 88 nm, indicating a deviation from the mean that is nearly 12 nm greater than the mean height. The S_{sk} was 0.0614, indicating that the majority of the values are slightly less than the S_a of 76.4 nm. The S_{ku} was 1.82, which signifies a variance resulting from regular, moderately-sized deviations from the mean. The Abbott-Firestone curve shows the distribution of various sub-phases that have been grouped into two primary phases, Phase 1 and Phase 2, as previously described. According to the curve, approximately 52 percent of the phase distribution is associated with Phase 1; whereas, roughly 48 percent of the phase distribution is related to Phase 2.

It is also observed that less than one percent of either phase would approach a S_p or S_v value.

Observation of the three-dimensional depiction of asphalt AAB provides visual corroboration and further details of the statistical analysis and Abbott-Firestone curve data presented previously. As shown in Figure 4.5, the majority of height values are associated with Phase 1, and most deviations of Phase 1 from the S_a are minor or insignificant. This indicates a relatively flat Phase 1 plane with a S_a of roughly 30 to 50 nm. Phase 2, in contrast, shows significant variability in height, which heavily influences the overall S_a of asphalt AAB. It is probable that all S_p and S_v values occur within Phase 2, and the S_a of Phase 2 is approximately 100 nm to 120 nm.

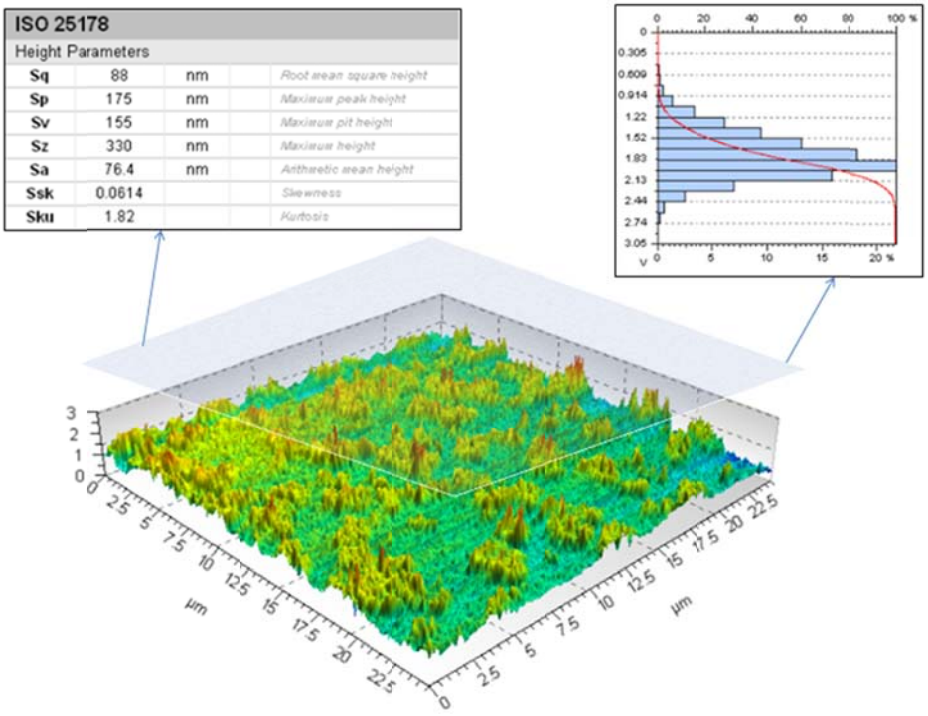

ISO 25178

Height Parameters

Sq	88	nm		Root mean square height
Sp	175	nm		Maximum peak height
Sv	155	nm		Maximum pit height
Sz	330	nm		Maximum height
Sa	76.4	nm		Arithmetic mean height
Ssk	0.0614			Skewness
Sku	1.82			Kurtosis

Figure 4.5. Three-dimensional depiction of asphalt AAB showing statistical analysis of surface texture and Abbott-Firestone curve.

As shown in Figure 4.6, ten creep measurements were taken randomly from each of the two phases. The results of the creep measurements are given as measured deflection in voltage versus time. The mean maximum deflection and standard deviation of deflection for Phase 1 were 0.30 V and 0.07 V, respectively; while, Phase 2 had a mean maximum deflection and deflection standard deviation of 0.21 V and 0.06 V, respectively. The distribution of the measurements for Phase 1 were fairly consistent, with the exception of two measurements, Phase 1-2 and Phase 1-5; however, these two measurements revealed the same upward trend as the overall data set for Phase 1 and are hence justifiable as accurate measurements contributing to the mean of Phase 1. Phase 2 showed slightly more variability between most of the measurements than those in Phase 1, but one noticeable indication of accurate measurements is the fact that seven of the ten measurements collected for Phase 2 fell below the lowest minimum deflection, 0.23 V, of Phase 1. These data provide strong indications of different material behavior amongst the two phases.

For comparison, the creep measurements taken in each of the two phases of asphalt AAB were averaged and superimposed onto the same graph as shown in Figure 4.7. The results show a significant difference in material behavior between the two phases. Phase 2 exhibits a higher stiffness than Phase 1, as indicated by a greater deflection under constant load. Furthermore, the deflection of Phase 1 after four seconds of creep was roughly 43 percent greater than the deflection of Phase 2.

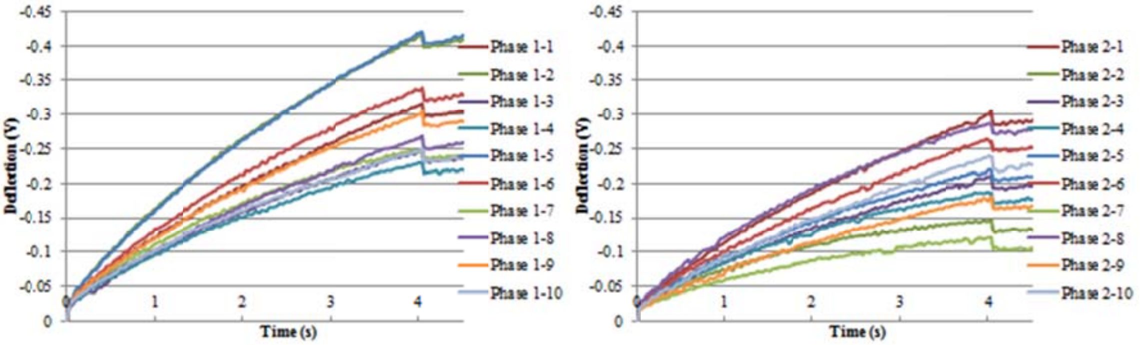

Figure 4.6. Creep measurements for asphalt AAB.

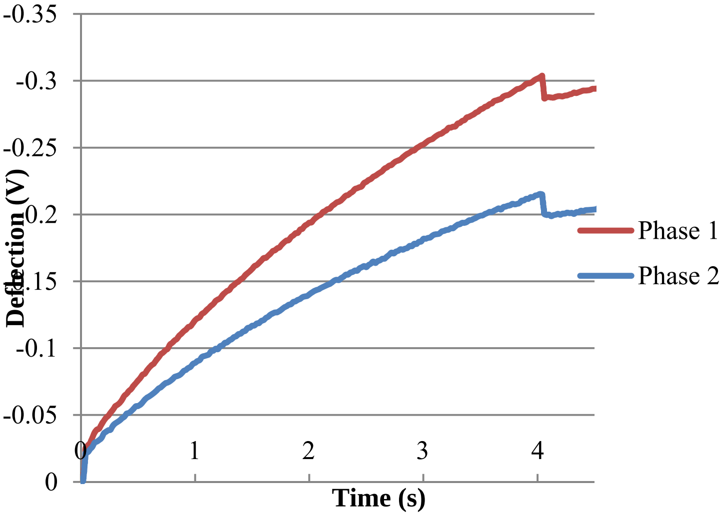

Figure 4.7. Superposition of average creep measurements for asphalt AAB.

4.2.2 Aged Asphalt AAB

Figure 4.8 presents a 25 by 25 μm phase image of aged asphalt AAB. As shown, three distinctive phases were identified. Similar to unaged asphalt AAB, the distribution of Phase 1 and Phase 2 appears to be random; however, a unique pattern is observed in which Phase 3 only exists directly within Phase 2. Also similar to asphalt AAB prior to aging, Phase 1 appears to be the dispersing phase and Phase 2 appears to be the dispersed phase. Phase 3, which has often been described as the “bee” phase by several researchers (Loeber et al., 1996; Pauli et al., 2001 and Mason et al., 2005), also appears to be part of the dispersed phase. Phase 3 also exhibits characteristic sharp variations in topography as shown in the profile extraction in Figure 4.8 and as formerly illustrated by Mason et al. (2005). Phase 2, which resembles an island of material, appears to dominate asphalt AAB after aging; whereas, Phase 1 only exists intermittently. Another noticeable trend amongst the phases is that Phase 2 appears to be interconnected, and Phase 1 and Phase 3 appear disconnected from other regions or entities. Additionally, Phase 3 is relatively cigar-shaped and varies in length between 1 and 4 µm.

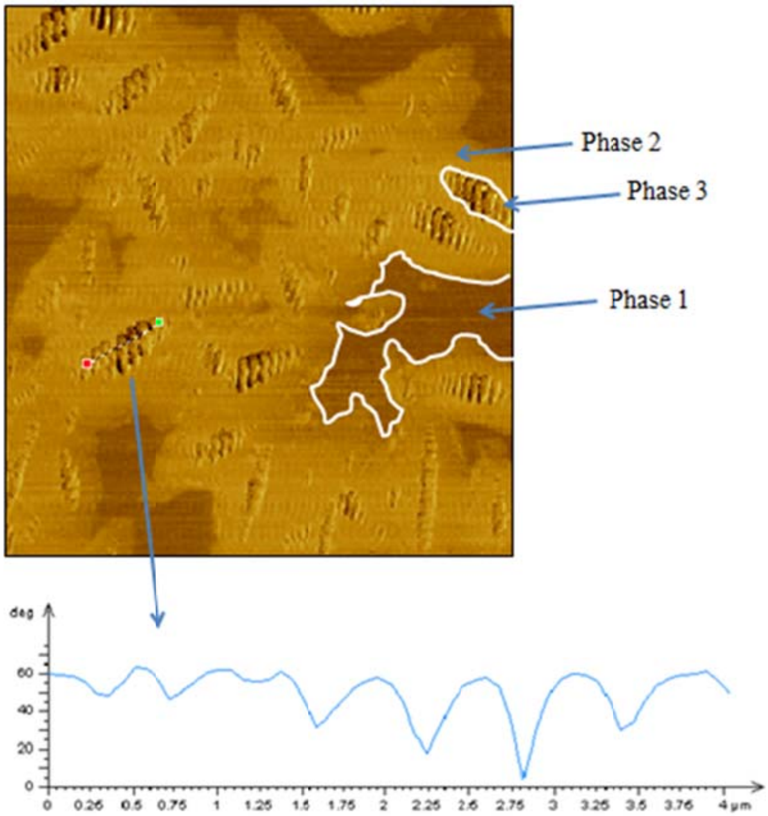

Figure 4.8. Phase image and profile extraction of aged asphalt AAB.

Figure 4.9 shows a three-dimensional depiction of aged asphalt AAB, including statistical analysis of surface texture and an Abbott-Firestone curve to describe the distribution of different phases. The statistical analysis indicates that S_p and S_v were 186 nm and 181 nm, respectively. S_z was 367 nm, which is nearly 40 nm greater than that of asphalt AAB prior to aging. S_a of the three distinctive phases was 72.7 nm. The S_q was 84.2 nm, signifying a deviation from the mean that is 11.5 nm greater than the mean height. The S_{sk} was -0.112, indicating that the majority of values are greater than the S_a of 72.7 nm. The S_{ku} was 1.88, which signifies a variance resulting from regular, moderately-sized deviations from the mean. According to the Abbott-Firestone curve and by observation, roughly 20 percent of the phase distribution would fall into the category of Phase 1; whereas, 70 percent and 10 percent of the phase distribution would be associated with Phase 2 and Phase 3, respectively.

Upon examination of the three-dimensional depiction of aged asphalt AAB in Figure 4.9, it is evident that Phase 1 and Phase 2 have only minor height deviations from their respective S_a values. This indicates relatively flat Phase 1 and Phase 2 planes with S_a values of roughly 30 to 50 nm and 60 to 75 nm, respectively. Conversely, Phase 3 shows significant variability in height. Furthermore, Phase 3 likely includes S_p and S_v values of the asphalt, and the S_a of Phase 3 is approximately 110 nm to 120 nm.

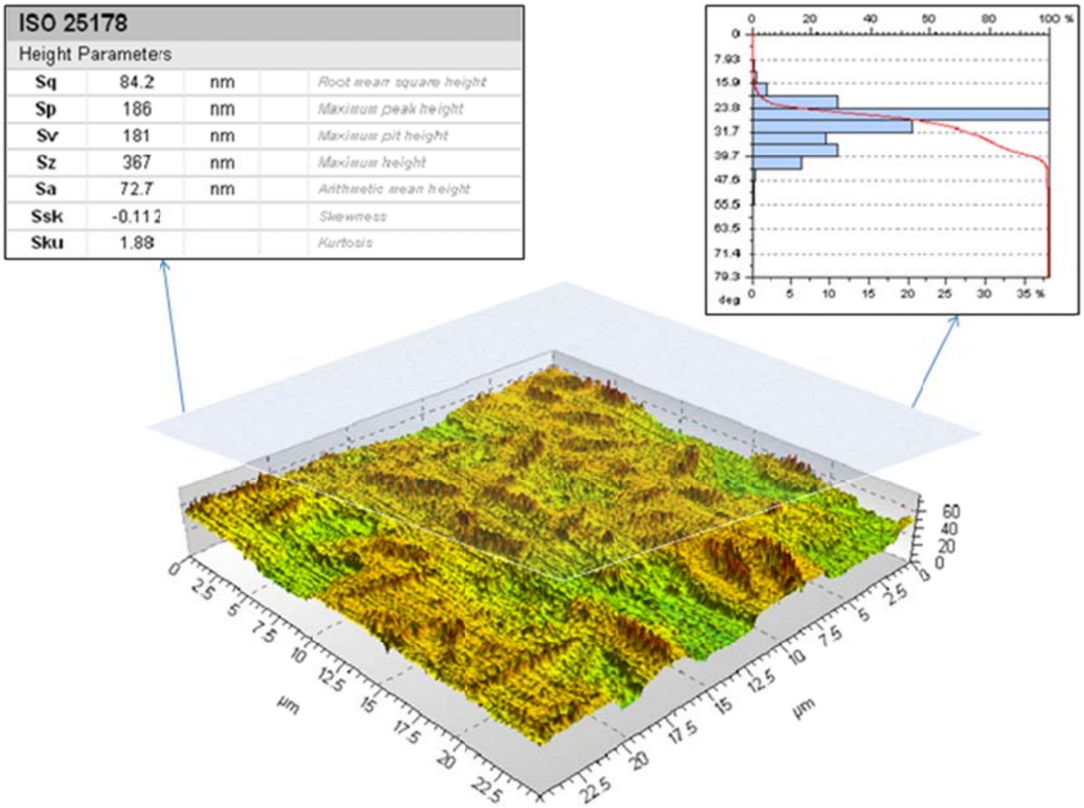

ISO 25178

Height Parameters

Sq	84.2	nm	Root mean square height
Sp	186	nm	Maximum peak height
Sv	181	nm	Maximum pit height
Sz	367	nm	Maximum height
Sa	72.7	nm	Arithmetic mean height
Ssk	-0.112		Skewness
Sku	1.88		Kurtosis

Figure 4.9. Three-dimensional depiction of aged asphalt AAB showing statistical analysis of surface texture and Abbott-Firestone curve.

As shown in Figure 4.10, ten creep measurements were taken randomly from each of the three phases. The mean maximum deflection and standard deviation of deflection for Phase 1 were 0.22 V and 0.07 V, respectively; while, Phase 2 had a maximum deflection and standard deviation of 0.18 V and 0.05 V, respectively. The mean maximum deflection and standard deviation of deflection for Phase 3 were 0.19 V and 0.08 V, respectively. As shown in Figure 4.10, the least amount of variability in data measurements occurred in Phase 2. Phase 2 force measurements ranged from roughly 0.10 to 0.25 V, and eight of ten measurements showed a deflection below 0.20 V. Six of ten measurements in Phase 1 showed a deflection greater than 0.20 V, which provides a strong indication of different material properties between the phases. The highest variability in data measurements occurred in Phase 3, which was anticipated due to the sharp changes in topography common to the phase and the inability to control whether a force measurement was taken in a high or low elevation location. To further support the notion that variability in Phase 3 force measurements was the result of major variations in topography, Figure 4.10 shows that few measurements were recorded near the mean maximum deflection value of 0.18 for Phase 3, but rather several measurements were recorded well above and below the mean.

The creep measurements taken in each the three phases of aged asphalt AAB were averaged and superimposed onto the same graph as shown in Figure 4.11. The results indicate a difference in material behavior between Phase 1 and Phase 2; however, Phase 3 shows very similar material behavior to Phase 2. Phase 2 and Phase 3 exhibit higher stiffness than Phase 1, as indicated by a smaller deflection under constant load. Additionally, the deflection of Phase 1 after four seconds of creep is roughly 22 percent greater than the deflection of Phase 2 and 16 percent greater than Phase 3. The representative force measurements of Phase 3 should be carefully interpreted, since it has been illustrated that two apparent sub-phases of sharply changing topography exist within Phase 3. The force measurements obtained from Phase 3 provide a valid indication of the contribution of the phase to the macro-behavior of asphalt, but the variability of measurements from this phase should be distinguished from other phases. The overall contribution of Phase 3 appears to weaken the asphalt by forming a lower stiffness zone within Phase 2.

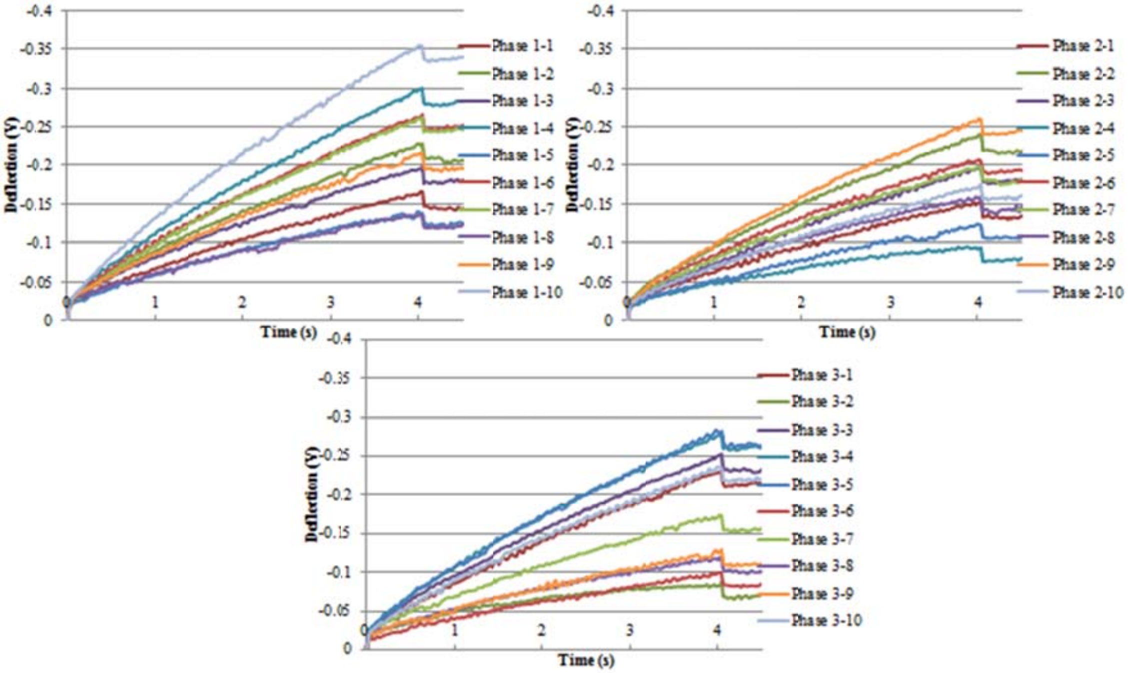

Figure 4.10. Creep measurements for aged asphalt AAB.

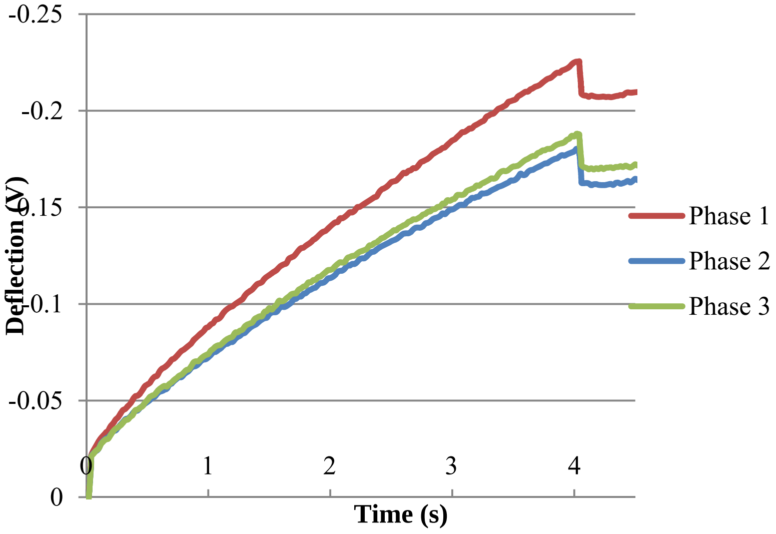

Figure 4.11. Superposition of average creep measurements for aged asphalt AAB.

4.2.3 Asphalt AAD

Figure 4.12 presents a 25 by 25 µm phase image of asphalt AAD. As shown, two distinctive phases were identified, and the distribution of the two phases was seemingly random. Similar to asphalt AAB prior to aging, the phases were identified as Phase 1 and Phase 2; whereas, Phase 1 and Phase 2 appear to be the dispersing phase and the dispersed phase, respectively. The overall size and shape of Phase 2 is somewhat variable, but the approximate longest dimension ranges from 1 to 4 µm. From the profile extraction, it is observed that certain Phase 2 entities resemble the "bee" structures that were detected by PDM as a third phase in aged asphalt AAB. The majority of Phase 2 entities, though, do not reveal such repetitious spikes of hills and valleys. It is also evident from the profile extraction that Phase 1 demonstrates a consistently flat topography.

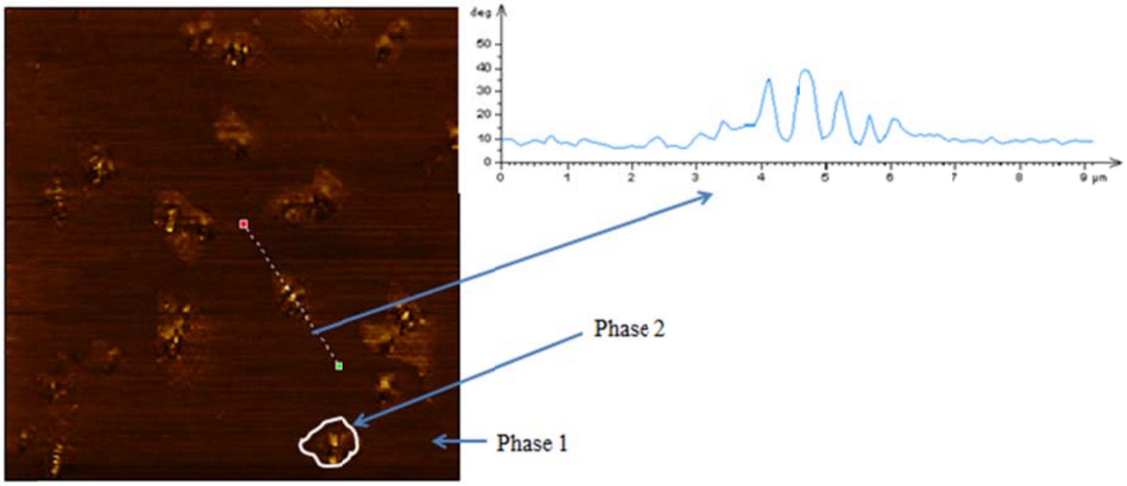

Figure 4.12. Phase image and profile extraction of asphalt AAD.

Figure 4.13 shows a three-dimensional depiction of asphalt AAD, including statistical analysis of surface texture and an Abbott-Firestone curve to describe the distribution of different phases. The statistical analysis indicates that S_p and S_v were both approximately 123 nm. The S_z of asphalt AAD was 245 nm, which is nearly 90 nm less than that of asphalt AAB. S_a of the two distinctive phases was 54.9 nm. The S_q was 63.4 nm, signifying a deviation from the mean that is 8.5 nm greater than the mean height. The S_{sk} was -0.0436, indicating that the majority of values are slightly greater than the S_a of 54.9 nm. The S_{ku} was 1.83, which signifies a variance resulting from regular, moderately-sized deviations from the mean. According to the Abbott-Firestone curve, nearly 85 percent of the phase distribution is related to Phase 1, and the remaining 15 percent of the phase distribution is associated with Phase 2.

Upon examination of the three-dimensional depiction of asphalt AAD in Figure 4.13, it is apparent that Phase 1 has only minor height deviations, which indicates a relatively flat Phase 1 plane with a S_a of roughly 30 to 50 nm. Conversely, Phase 2 shows significant variability in height but exists only intermittently and, therefore, has limited effects on the overall S_a of asphalt AAD. Phase 2 likely includes the S_p and S_v values of the asphalt, and the S_a of Phase 3 is approximately 70 to 90 nm. It is also observed that significantly less than one percent of the asphalt surface approaches S_p and S_v values.

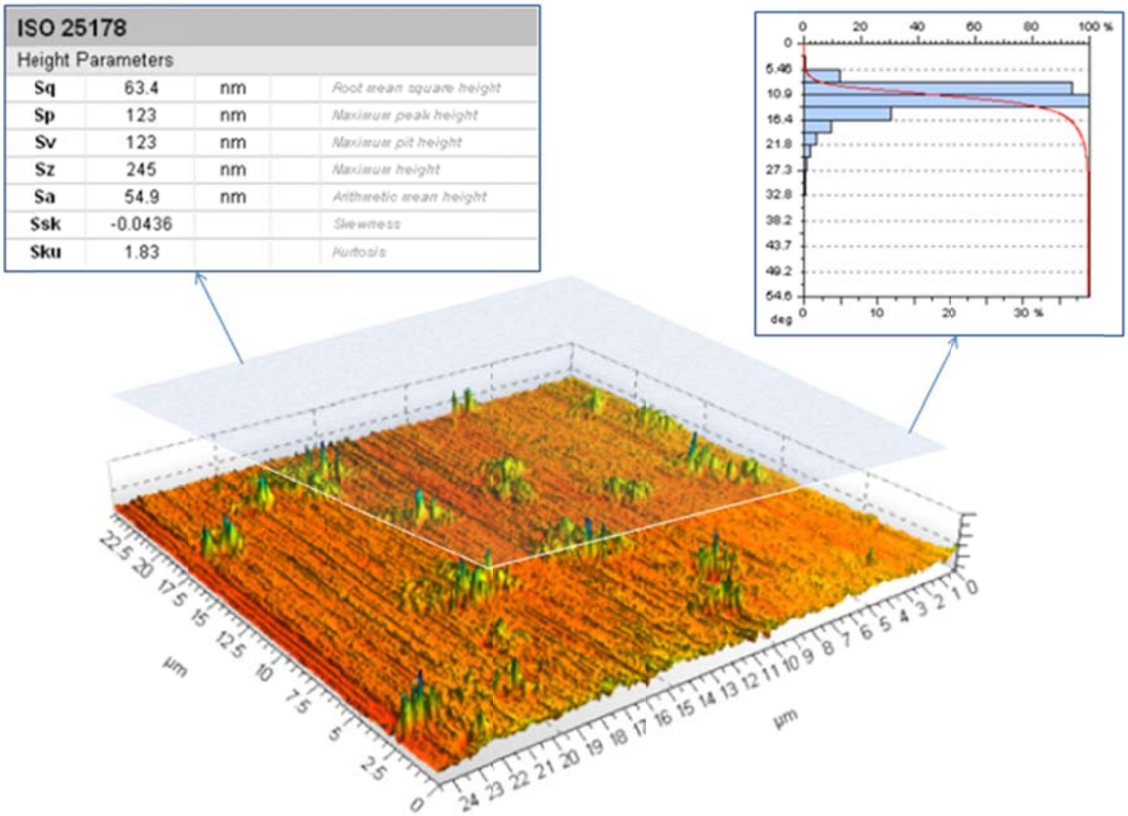

ISO 25178

Height Parameters

Sq	63.4	nm		Root mean square height
Sp	123	nm		Maximum peak height
Sv	123	nm		Maximum pit height
Sz	245	nm		Maximum height
Sa	54.9	nm		Arithmetic mean height
Ssk	-0.0436			Skewness
Sku	1.83			Kurtosis

Figure 4.13. Three-dimensional depiction of asphalt AAD showing statistical analysis of surface texture and Abbott-Firestone curve.

As shown in Figure 4.14, ten creep measurements were taken randomly from each of the two phases. The mean maximum deflection and standard deviation of deflection for Phase 1 were 0.48 V and 0.11 V, respectively; while, Phase 2 had a mean maximum deflection and deflection standard deviation of 0.28 V and 0.17 V, respectively. Such high standard deviations from the mean for each phase caused some concern, but after closer inspection of the data measurements, common trends amongst each data set seems to indicate a clear difference in material properties, nonetheless. Though high variability was revealed amongst the force measurements from Phase 1, all measurements yielded deflections greater than 0.27 V, and seven of ten measurements exhibited a deflection greater than 0.45 V. Consequently, seven of ten measurements from Phase 2 yielded a deflection less than 0.27 V. As for the other three measurements collected from Phase 2, it is suspected that the measurements are erroneous and misrepresentative of the material behavior of Phase 2. This notion is closely supported by similarities of the three measurements to the majority of measurements from Phase 1. It is possible that the three force measurements in question were mistakenly taken at or near a boundary between the two phases and yielded values that were more representative of the material behavior of Phase 1; nonetheless, by including the questionable measurements as part of the mean for Phase 2, a conclusive difference between the material behavior of the two phases is still evident.

For comparison, the creep measurements taken in each of the two phases of asphalt AAD were averaged and superimposed onto the same graph as shown in Figure 4.15. The results indicate a sizeable difference in material behavior between the two phases. Phase 2 exhibits a higher stiffness than Phase 1, as indicated by a smaller deflection under constant load. Furthermore, the deflection of Phase 1 after four seconds of creep is roughly 42 percent greater than the deflection of Phase 2.

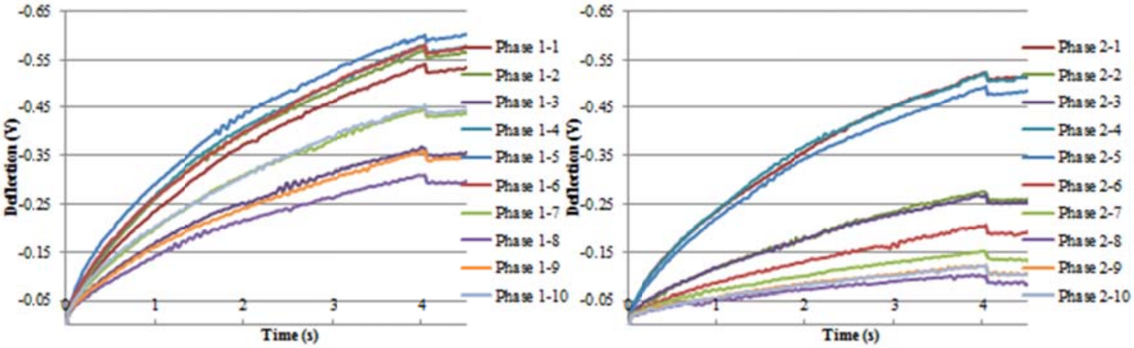

Figure 4.14. Creep measurements for asphalt AAD.

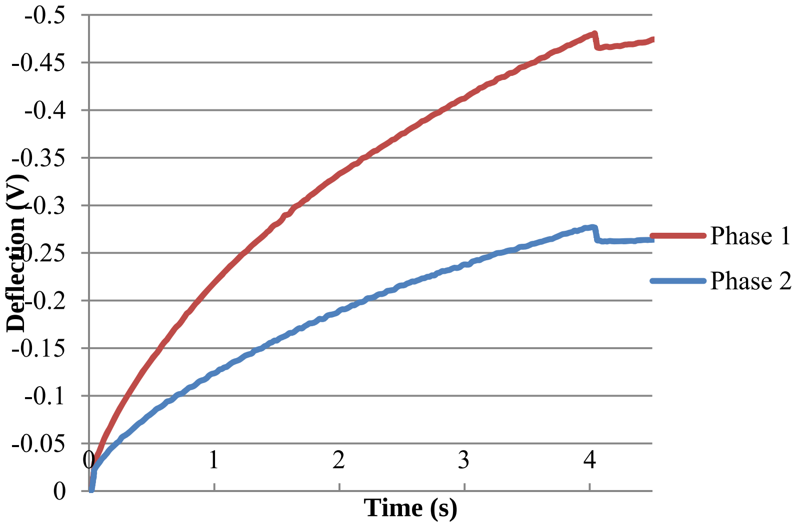

Figure 4.15. Superposition of average creep measurements for asphalt AAD.

4.2.4 Aged Asphalt AAD

Figure 4.16 presents a 25 by 25 µm phase image of aged asphalt AAD. As shown, three distinctive phases were identified. Similar to aged asphalt AAB, the distribution of Phase 1 and Phase 2 appears to be random; however, a unique pattern is observed in which Phase 3 only exists directly within Phase 2. Also similar to aged asphalt AAB, Phase 1 appears to be the dispersing phase, while Phase 2 and Phase 3 appear to be dispersed phases. Phase 3 for aged asphalt AAD also resembles the characteristic “bee” structure as was apparent in aged asphalt AAB; yet, one clear difference between the Phase 3 structure of the two asphalts is the significant dissimilarity in size of each entity. While the cigar-shape and discontinuity of each entity is still evident, the length of each structure has substantially increased from 1 to 4 µm for aged asphalt AAB to roughly 5 to 11 µm for the majority of “bee” structures in aged asphalt AAD. The same variations in topography for the bee structures that were observed in aged asphalt AAB and sporadically in asphalt AAD prior to aging are also observed for aged asphalt AAD. The combination of Phase 2 and Phase 3 dominate asphalt AAD after aging; whereas, Phase 1 only nominally exists; whereas, prior to aging, Phase 1 comprised roughly 85 percent of the area. A further observation is that Phase 2 appears to be interconnected, and Phase 1 and Phase 3 appear disconnected from other regions or entities, with few exceptions.

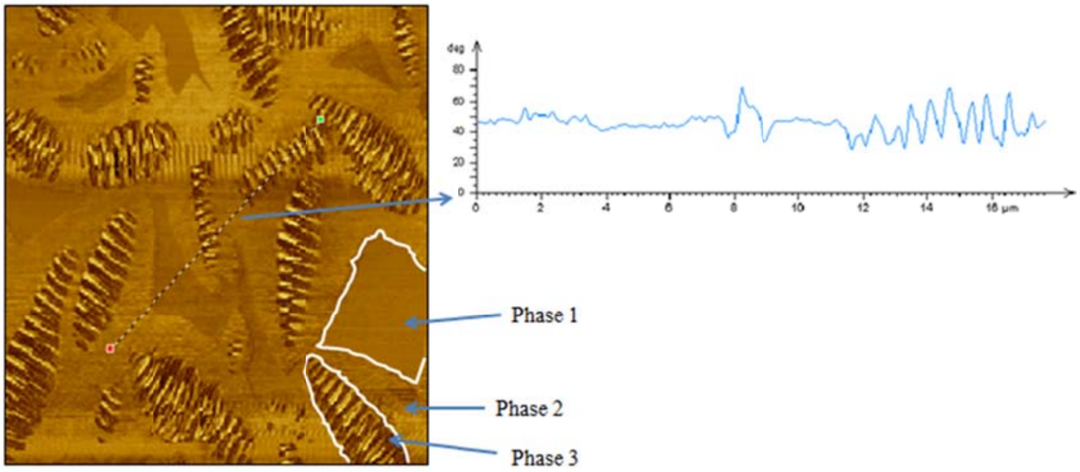

Figure 4.16. Phase image and profile extraction of aged asphalt AAD.

Figure 4.17 shows a three-dimensional depiction of aged asphalt AAD, including statistical analysis of surface texture and an Abbott-Firestone curve to describe the distribution of different phases. The statistical analysis indicates that S_p and S_v are 134 nm and 154 nm, respectively. S_z was 288 nm, which is roughly 40 nm greater than that of asphalt AAD prior to aging. S_a of the three distinctive phases was 54.2 nm. The S_q was 62 nm, signifying a deviation from the mean that is 7.8 nm greater than the mean height. The S_{sk} was -0.227, indicating that the majority of values are greater than the S_a of 54.2 nm. The S_{ku} was 1.87, which signifies a variance resulting from regular, moderately-sized deviations from the mean. According to the Abbott-Firestone curve, roughly 17 percent of the phase distribution is related to Phase 1; whereas, 45 percent and 38 percent of the phase distribution is associated with Phase 2 and Phase 3, respectively.

Upon examination of the three-dimensional depiction of aged asphalt AAD in Figure 4.17, it was evident that Phase 1 and Phase 2 had only minor height deviations from their respective S_a values. This familiar trend was also previously observed in aged asphalt AAB. This indicates relatively flat Phase 1 and Phase 2 planes with S_a values of roughly 10 to 30 nm and 40 to 50 nm, respectively. Conversely, Phase 3 consistently shows significant variability in height amongst each entity. From these observations it is probable that Phase 3 includes several peaks and pits approaching S_p and S_v values of the asphalt, and the S_a of Phase 3 is approximately 70 nm to 80 nm.

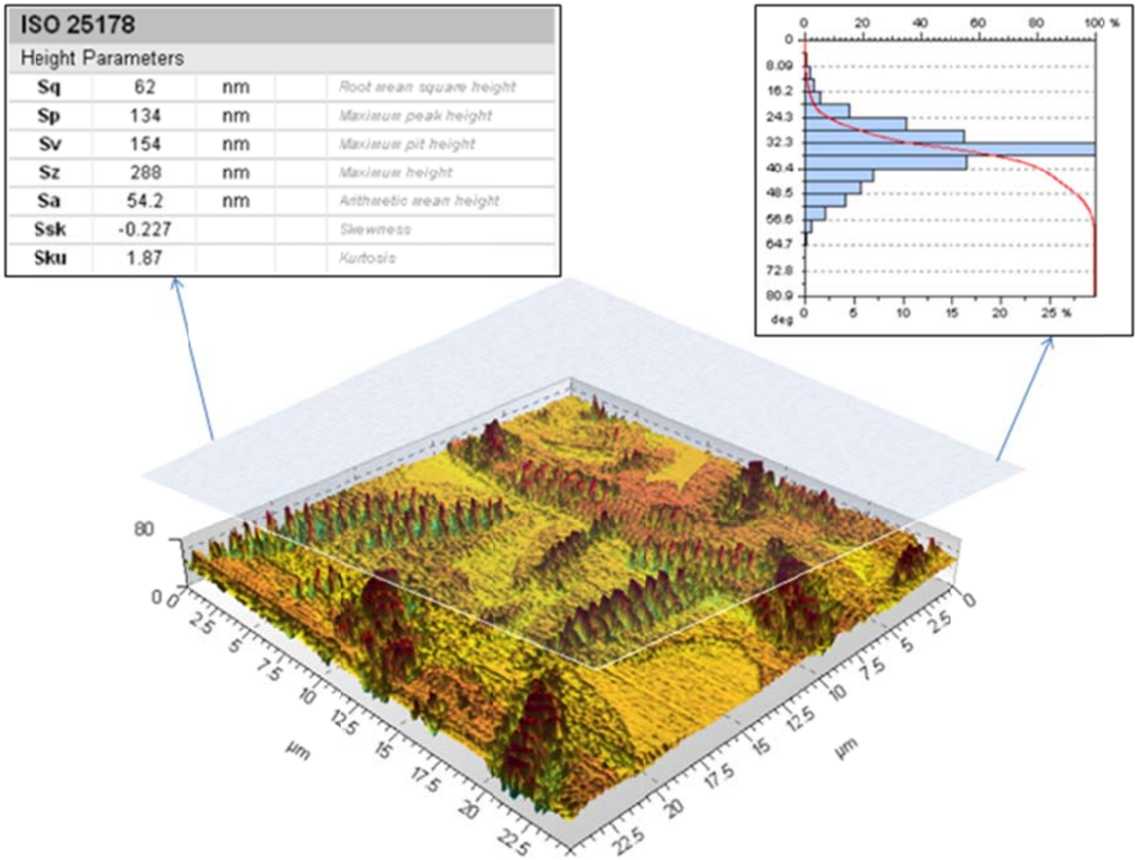

ISO 25178			
Height Parameters			
Sq	62	nm	Root mean square height
Sp	134	nm	Maximum peak height
Sv	154	nm	Maximum pit height
Sz	288	nm	Maximum height
Sa	54.2	nm	Arithmetic mean height
Ssk	-0.227		Skewness
Sku	1.87		Kurtosis

Figure 4.17. Three-dimensional depiction of aged asphalt AAD showing statistical analysis of surface texture and Abbott-Firestone curve.

As shown in Figure 4.18, ten creep measurements were taken randomly from each of the three phases. The mean maximum deflection and standard deviation of deflection for Phase 1 were 0.20 V and 0.03 V, respectively; while, Phase 2 had a mean maximum deflection and deflection standard deviation of 0.12 V and 0.05 V, respectively. The mean maximum deflection and standard deviation of deflection for Phase 3 were 0.16 V and 0.03 V, respectively. The precision of the data measurements collected for aged asphalt AAD was remarkable. All ten force measurements obtained for Phase 1 exhibited maximum deflection values greater than 0.17 V; whereas, all ten force measurements collected for Phase 2 were revealed maximum deflection values less than 0.17 V. This clearly draws a line in which material behavior is dissimilar amongst the two phases. The force measurements for Phase 3 were also very precise, but the same trend previously observed for Phase 3 of aged asphalt AAB was observed in this case as well. Although the ten measurements taken in Phase 3 had minimal deviation from the mean value of 0.16V, further observation of Figure 4.18 reveals that virtually no measurements occur near the mean value. There appears to be two distinctive locations within Phase 3 that consistently exhibit different material properties, but due to the small size of these varying structures within Phase 3, it would be nearly impossible to distinguish the force measurements between these locations.

The creep measurements taken in each the three phases of aged asphalt AAD were averaged and superimposed onto the same graph as shown in Figure 4.19. It is apparent that results show a significant difference in material behavior between each of the three phases. In agreement with prior results, Phase 1, or the seemingly dispersing phase, exhibited the lowest stiffness of the three phases. As with aged asphalt AAB, Phase 2 exhibited the highest stiffness, and Phase 3 demonstrated a moderate stiffness. A further observation of Phase 3 in aged asphalt AAD is that a considerably larger contrast in stiffness from Phase 2 is evident when compared to aged asphalt AAB. This suggests that Phase 2 and Phase 3 of aged asphalt AAD share less commonalities in terms of material behavior than the equivalent phases of aged asphalt AAB. Furthermore, the deflection of Phase 1 after four seconds of creep is roughly 67 percent greater than the deflection of Phase 2 and 25 percent greater than Phase 3.

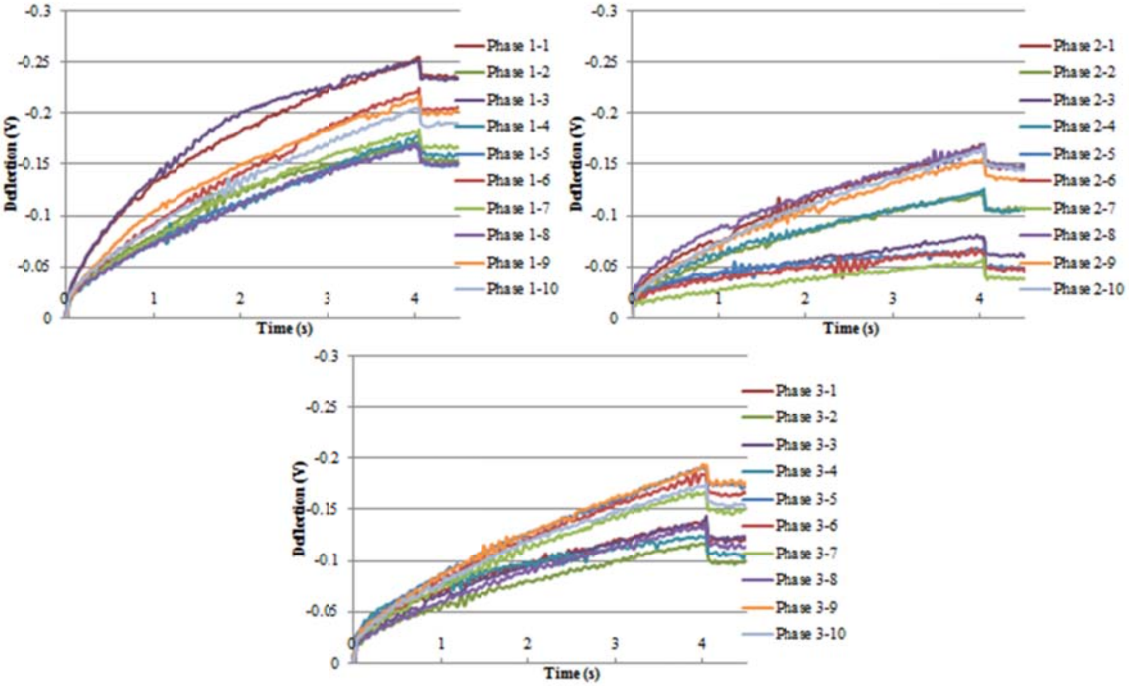

Figure 4.18. Creep measurements for aged asphalt AAD.

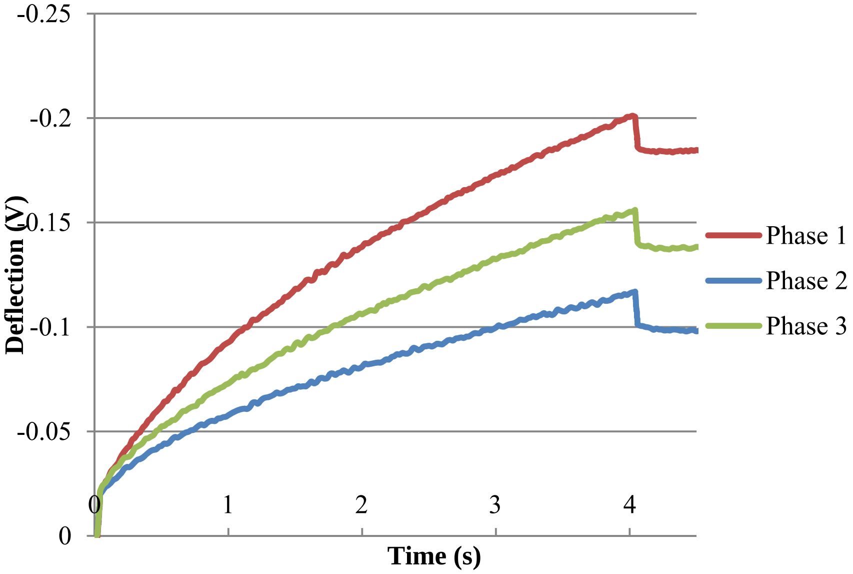

Figure 4.19. Superposition of average creep measurements for aged asphalt AAD.

4.2.5 Asphalt ABD

Figure 4.20 presents a 25 by 25 µm phase image of asphalt ABD. As shown, two distinctive phases were identified, and the distribution of the two phases was seemingly random. Unlike asphalt AAB and asphalt AAD, a distribution of noticeably different structural phases was not apparent in the PDM images obtained for asphalt ABD, despite numerous attempts to obtain such an image. One noticeable difference, nonetheless, within the mostly continuous medium of asphalt ABD was the distribution of light and dark shades of the same color. It was not apparent prior to performing creep measurements, whether the different shades were the result of different film thickness at these locations or due to possible material differences; subsequently, the dispersal of these shades was used as the basis for identification of two separate phases to test for potentially different material behavior among them. The two phases were identified as Phase 1 and Phase 2, and as indicated in the profile extraction, the two phases exhibited a consistently varying topography as previously seen within the "bee" structures of aged asphalts AAB and AAD.

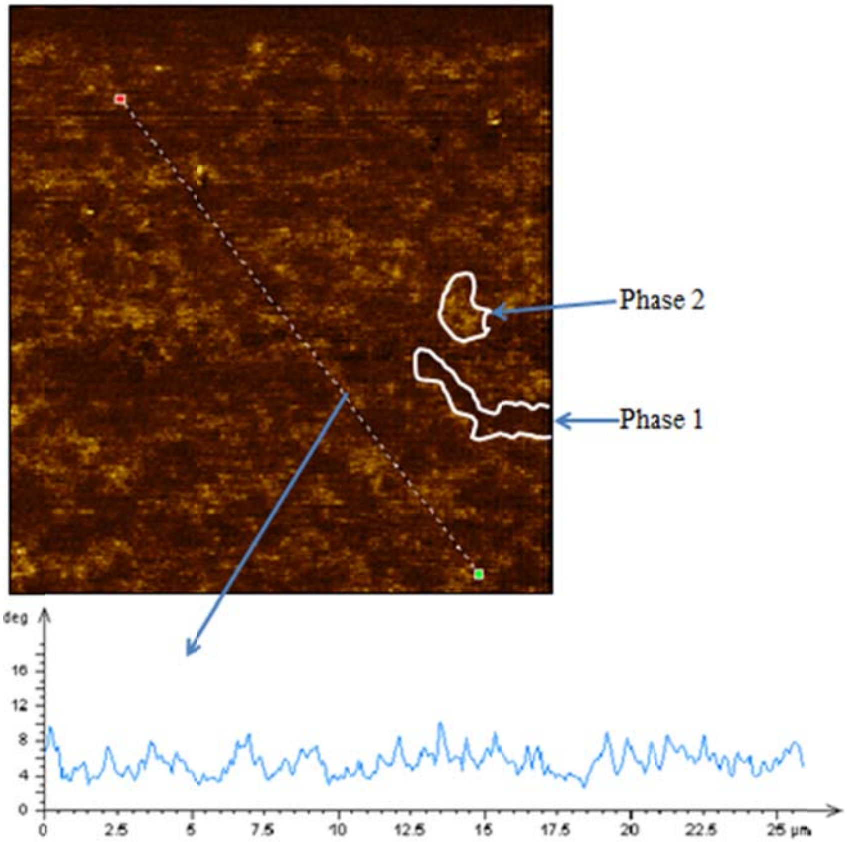

Figure 4.20. Phase image and profile extraction of asphalt ABD.

Figure 4.21 shows a three-dimensional depiction of asphalt AAD, including statistical analysis of surface texture and an Abbott-Firestone curve to describe the distribution of different phases. The statistical analysis indicates that S_p and S_v are 73.8 nm and 82.9 nm, respectively. The S_z of asphalt AAD is 157 nm, which is nearly 90 nm less than that of asphalt AAD and approximately 170 nm less than asphalt AAB. S_a of the two distinctive phases is 35.3 nm.

The S_q is 40.8 nm, signifying a deviation from the mean that is 5.5 nm greater than the mean height. The S_{sk} was -0.0505, indicating that the majority of values are slightly greater than the S_a of 35.3 nm. The S_{ku} was 1.31, which signifies a variance that results from frequent, minor deviations from the mean. According to the Abbott-Firestone curve, nearly 48 percent of the phase distribution is associated of Phase 1, and the remaining 52 percent of the phase distribution is related to Phase 2.

Upon examination of the three-dimensional depiction of asphalt ABD in Figure 4.21, it is apparent that smaller and more frequent height deviations are common amongst the two phases, as indicated by a lower S_{ku} value. Both phases show significant variability in height; whereas, Phase 1 likely contains values approaching the S_v of the asphalt, and Phase 2 is comprised of values approaching the S_p. The S_a of Phase 1 and Phase 2 are approximately 20 nm and 50 nm, respectively.

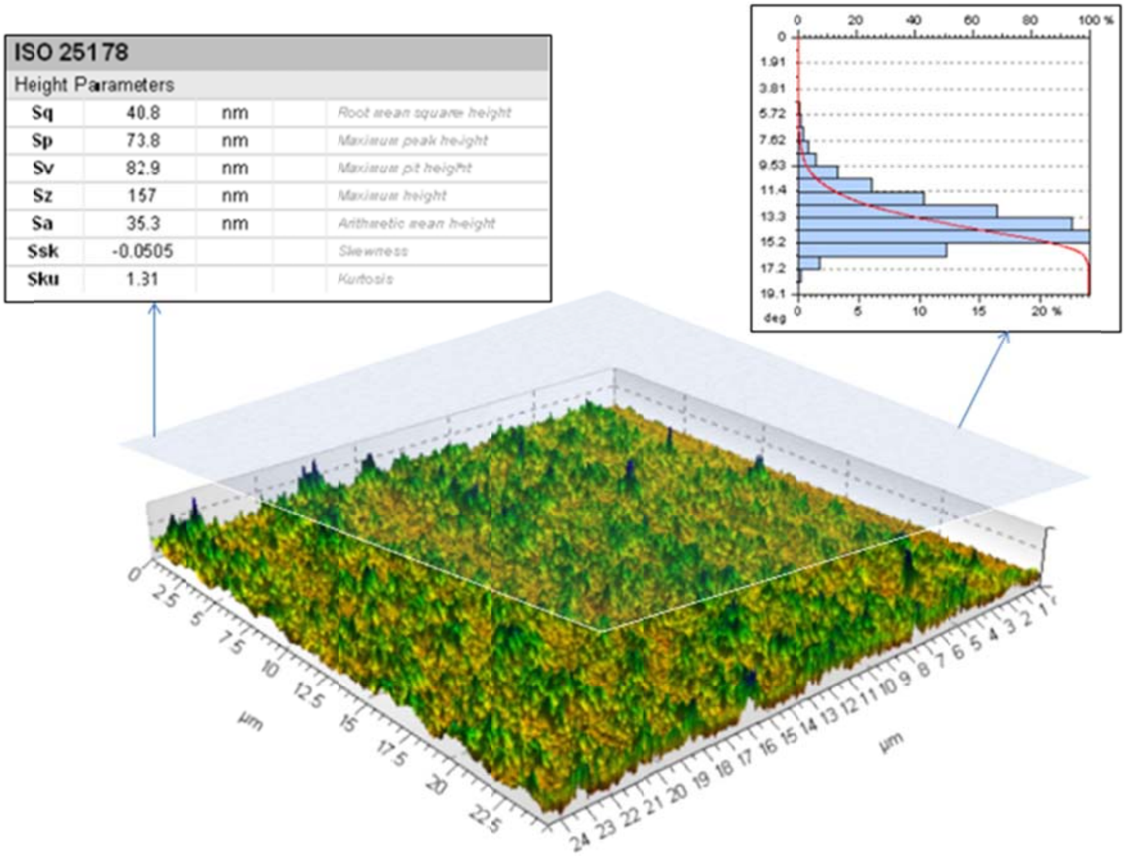

ISO 25178				
Height Parameters				
Sq	40.8	nm		Root mean square height
Sp	73.8	nm		Maximum peak height
Sv	82.9	nm		Maximum pit height
Sz	157	nm		Maximum height
Sa	35.3	nm		Arithmetic mean height
Ssk	-0.0505			Skewness
Sku	1.31			Kurtosis

Figure 4.21. Three-dimensional depiction of asphalt ABD showing statistical analysis of surface texture and Abbott-Firestone curve.

As shown in Figure 4.22, ten creep measurements were taken randomly from each of the two phases. The mean maximum deflection and standard deviation of deflection for Phase 1 were 0.27 V and 0.02 V, respectively; while, Phase 2 had a mean maximum deflection and deflection standard deviation of 0.18 V and 0.05 V, respectively. A high precision of force measurements is apparent in Phase 1, in which all maximum deflection values range from only 0.24 to 0.30 V. The force measurements from Phase 2 show more variability, but still show a noticeable difference in material behavior as indicated by eight of ten force measurements exhibiting deflection values less than 0.21 V. This indicates that the different shades of color revealed in the phase image were representative of different phases with different material properties. As previously observed in Phase 2 of asphalt AAD, a couple of the measurements collected from Phase 2 of asphalt ABD are suspected to be erroneous and misrepresentative of the material behavior of Phase 2. It is possible that the two force measurements in question were mistakenly taken at or near a boundary between the two phases and yielded values that were more representative of the material behavior of Phase 1, and this is clearly supported by similarities of the two measurements to the majority of measurements from Phase 1.

For comparison, the creep measurements taken in each of the two phases of asphalt AAB were averaged and superimposed onto the same graph as shown in Figure 4.23. The results show a considerable difference in material behavior between the two phases, despite inclusion of the two suspected erroneous force measurements from Phase 2. Phase 2 exhibits a higher stiffness than Phase 1, as indicated by a smaller deflection under constant load. Furthermore, the deflection of Phase 1 after four seconds of creep is roughly 50 percent greater than the deflection of Phase 2.

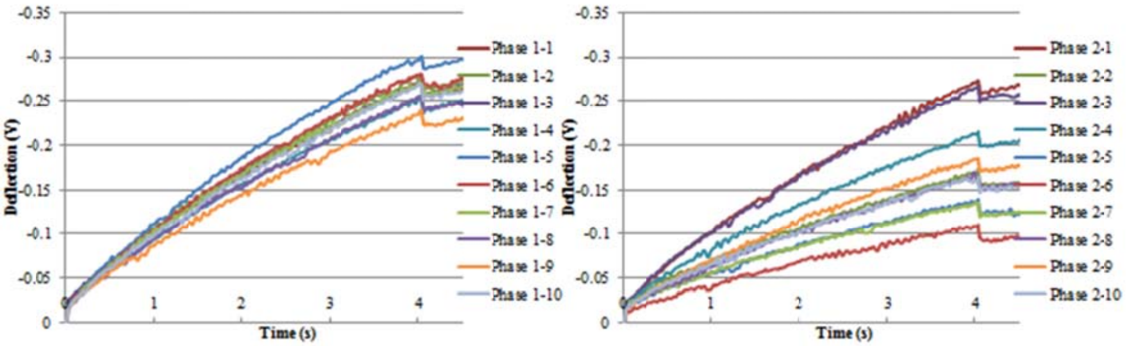

Figure 4.22. Creep measurements for asphalt ABD.

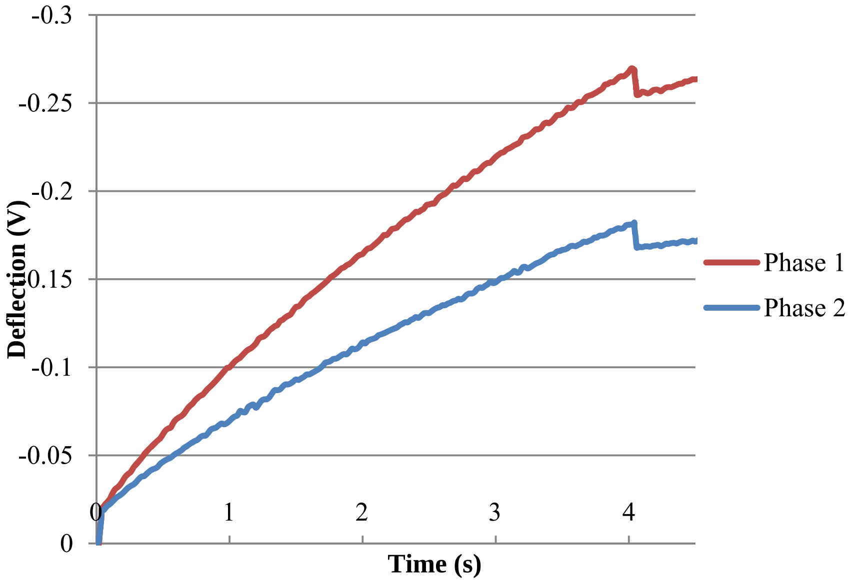

Figure 4.23. Superposition of average creep measurements for asphalt ABD.

4.2.6 Aged Asphalt ABD

Figure 4.24 presents a 25 by 25 μm phase image of aged asphalt ABD. As shown, two distinctive phases were identified, and the distribution of the two phases was seemingly random. As with asphalt ABD prior to aging, a distribution of noticeably different structural phases was not apparent in the PDM images obtained for aged asphalt ABD. Additionally, the apparent structural changes induced by aging asphalts AAB and AAD were not observed for asphalt ABD. The same method used to identify two phases for asphalt ABD prior to aging was also used for aged asphalt ABD. The primary phase change that was observed due to aging asphalt ABD is an increased percentage of Phase 2 and a subsequent decrease in Phase 1. It was also observed in the profile extraction that a spike in topography between Phase 1 and Phase 2 was much more evident than detected prior to aging. A commonality, though, to asphalt ABD prior to aging is the consistently varying topography observed throughout the specimen. Based on the increased topography spikes between the phases and the overall percentage increase of Phase 2 due to aging, some indication of structural change in asphalt ABD seems evident, although not entirely apparent in the phase image.

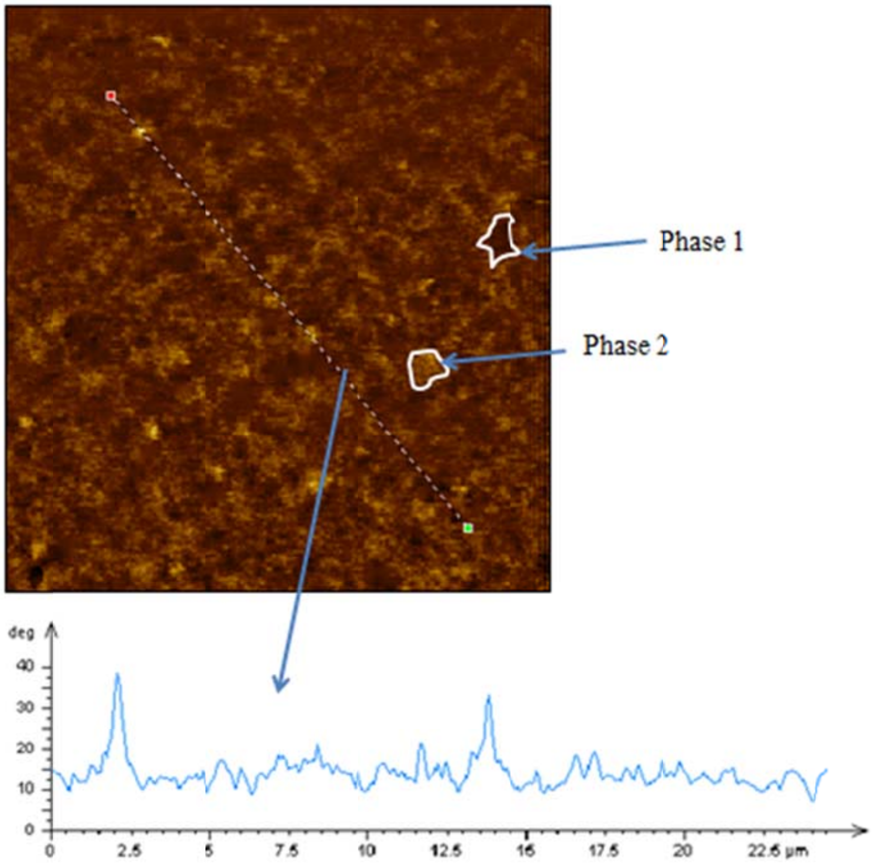

Figure 4.24. Phase image and profile extraction of aged asphalt ABD.

Figure 4.25 shows a three-dimensional depiction of aged asphalt ABD, including statistical analysis of surface texture and an Abbott-Firestone curve to describe the distribution of different phases. The statistical analysis indicates that S_p and S_v were 152 nm and 175 nm, respectively. The S_z of asphalt AAD was 327 nm, which is approximately double that of asphalt ABD prior to aging. S_a of the two distinctive phases was 63.7 nm. The S_q was 74.6 nm, signifying a deviation from the mean that is 10.9 nm greater than the mean height. The S_{sk} was -0.128, indicating that the majority of values are greater than the S_a of 63.7 nm. The S_{ku} was 2.02, which signifies a variance that results from occasional, large deviations from the mean. According to the Abbott-Firestone curve, nearly 41 percent of the phase distribution falls into the category of Phase 1, and the remaining 59 percent of the phase distribution is associated with Phase 2.

Upon examination of the three-dimensional depiction of aged asphalt ABD in Figure 4.25, it was apparent that the two phases are intermittently distributed and exhibiting significant height variability; however, a high S_{ku} value suggested otherwise. This discrepancy illustrates the importance of having statistical, graphical and visual data to fully assess the characteristics of asphalt microstructures. Closer inspection of the three-dimensional image of aged asphalt ABD revealed that the height distribution was actually quite consistent within each phase with the exception of a few peaks and pits. The overall consistency of each phase height is difficult to detect due to the consistently erratic distribution of the two phases, but the consistency is substantiated by a high S_{ku} value and the distribution shown in the Abbott-Firestone curve. Phase 1 likely contains values approaching the S_v of the asphalt, and Phase 2 is comprised of values approaching the S_p. The S_a values of Phase 1 and Phase 2 are approximately 40 nm and 80 nm, respectively.

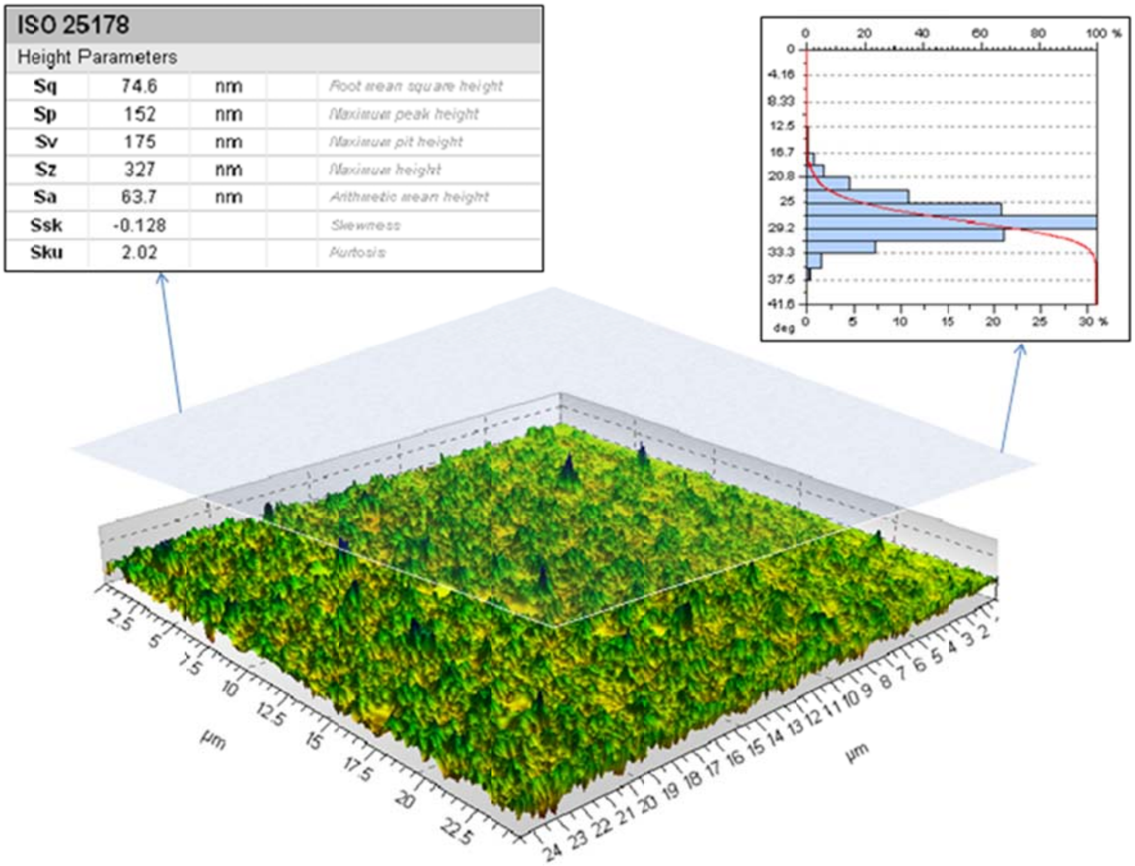

ISO 25178

Height Parameters

Sq	74.6	nm		Root mean square height
Sp	152	nm		Maximum peak height
Sv	175	nm		Maximum pit height
Sz	327	nm		Maximum height
Sa	63.7	nm		Arithmetic mean height
Ssk	-0.128			Skewness
Sku	2.02			Kurtosis

Figure 4.25. Three-dimensional depiction of aged asphalt ABD showing statistical analysis of surface texture and Abbott-Firestone curve.

As shown in Figure 4.26, ten creep measurements were taken randomly from each of the two phases. The mean maximum deflection and standard deviation of deflection for Phase 1 were 0.10 V and 0.004 V, respectively; while, Phase 2 had a mean maximum deflection and deflection standard deviation of 0.08 V and 0.01 V, respectively. The force measurements collected for Phase 1 were extremely precise. The maximum deflection values only ranged from 0.09 to 0.11 V. The force measurements obtained for Phase 2 were also very precise, with the exception of two measurements. Eight of ten measurements exhibited maximum deflection values ranging only from 0.07 to 0.09 V, which clearly illustrates different, although minor, material behavior between the two phases. It is likely that the two measurements that fall outside of the 0.07 to 0.09 V range of remaining Phase 2 measurements are erroneous and misrepresentative of the material behavior of Phase 2. As illustrated in previous cases, it is possible that the two force measurements in question were mistakenly taken at or near a boundary between the two phases and yielded values that were more representative of the material behavior of Phase 1. This perception is supported by similarity of the two measurements to the majority of measurements from Phase 1.

The creep measurements taken in each of the two phases of asphalt AAB were averaged and superimposed onto the same graph as shown in Figure 4.27. The results indicate a less significant difference in material behavior between the two phases than that observed prior to aging, although Phase 2 still exhibits a higher stiffness than Phase 1. Moreover, the deflection of Phase 1 after four seconds of creep is roughly 25 percent greater than the deflection of Phase 2.

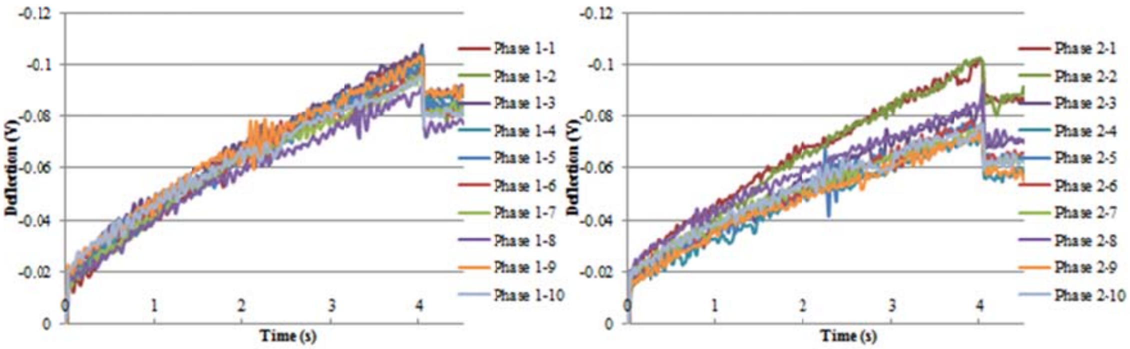

Figure 4.26. Creep measurements for aged asphalt ABD.

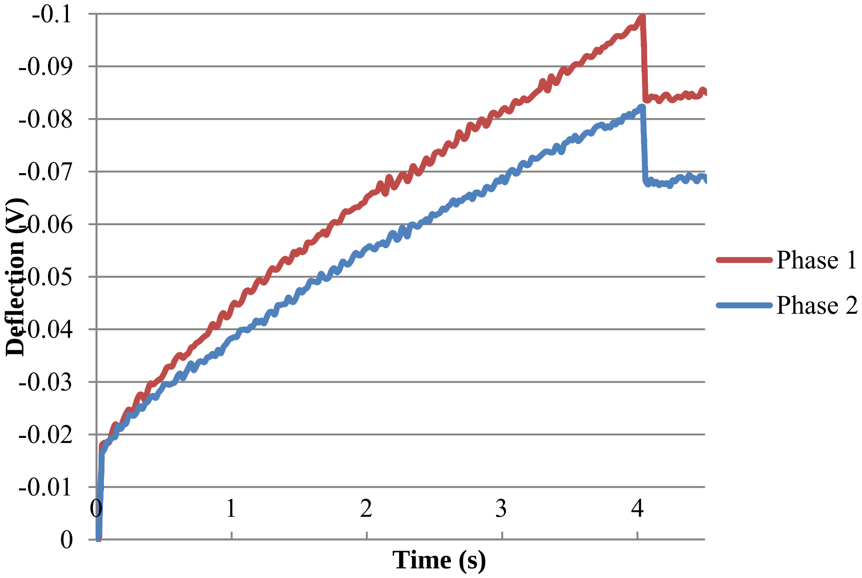

Figure 4.27. Superposition of average creep measurements for aged asphalt ABD.

4.3 OVERALL ANALYSIS AND COMPARISONS

As presented in this section, phase images, profile extractions, three-dimensional phase depictions, surface texture statistical analysis, graphical phase distribution and creep measurements were produced and analyzed as the basis of a comprehensive study of micromechanical properties of asphalt. Since asphalt is a complex material that undergoes significant changes due to aging, it was also important to evaluate the extent of these structural and mechanical changes during the aging process. This portion of the section consists of the overall analysis and comparisons of findings presented thus far.

Although asphalt micro-phase topography was not originally a primary focus of this experiment, the unearthing of obvious correlations between topography and phase change during preliminary stages of this study made a thorough analysis of surface roughness characteristics essential to appropriately assess microstructural phase differences of each asphalt. It was originally believed that many topography differences detected from asphalt thin-film specimens were likely due to uneven thin-film distributions and could, hence, be neglected in a study involving isolation of phases and force measurements. While some of the surface roughness and topography fluctuations observed in topography images are directly related to variability introduced during specimen preparation, there are irrefutable patterns that have been demonstrated as having a direct link between surface topography and phase change. Table 4.1 provides a summary of the surface texture statistical analysis for each of the asphalts studied during this experiment.

Table 4.1. Comparison of Surface Texture Statistical Analysis.

Asphalt	Surface Texture Statistics						
	S_p (nm)	S_v (nm)	S_z (nm)	S_a (nm)	S_q (nm)	S_{sk}	S_{ku}
AAB	175	155	330	76.4	88.0	0.06	1.82
AAB-aged	186	181	367	72.7	84.2	-0.11	1.88
AAD	123	123	245	54.9	63.4	-0.04	1.83
AAD-aged	134	154	288	54.2	62.0	-0.23	1.87
ABD	74	83	157	35.3	40.8	-0.05	1.31
ABD-aged	152	175	327	63.7	74.6	-0.13	2.02

A notable observation from the comparison of surface texture statistics is that S_p, S_v and S_z increased for each asphalt due to aging, which clearly shows that age-induced structural phase change is also accompanied by increased roughness. A sizeable increase in roughness was statistically observed for asphalt ABD, but an indistinguishable phase image made visual scrutiny of this transformation difficult. An overall reduction in S_a and S_q in asphalt AAB and asphalt AAD indicates that Phase 2 becomes more dispersed with age, especially since Phase 2 topography is quite variable prior to aging and relatively flat after aging. This notion is also supported by observing the phase images of asphalts AAB and AAD before and after aging as shown in Figures 4.28 and 4.29, respectively. While the phase images of asphalt ABD were inconclusive, the statistical data for asphalt ABD specifies a significant increase in S_a and S_q after aging, which suggests that molecular clustering occurs during the aging process. Such clustering is also observed for asphalt AAB and asphalt AAD after aging by the marked presence of the “bee” structures; however, the dispersion of Phase 2 in the case of asphalts AAB and AAD appears to balance the average surface parameters so that the statistical values more closely match their respective values prior to aging. This further indicates that unlike asphalts AAB and AAD, phase dispersion is most likely not occurring in asphalt ABD during aging. With the exception of unaged asphalt AAB, the S_{sk} of each asphalt indicates that the majority of the height distribution is greater than the S_a. This notion is substantiated by the Phase 3 peaks observed in aged asphalt AAB and aged asphalt AAD phase images and also by the number of peaks observed in three-dimensional depictions of aged and unaged asphalt ABD.

As this experiment supports, long-term aging clearly induces microstructural changes in asphalt. The form and extent of these changes, however, were different for each asphalt. The following three types of microstructural changes, or associations of molecules into distinctive patterns, were observed during this study: dispersion of phase, clustering of phase and materialization of phase.

Figure 4.28 demonstrates the extensive microstructural change that asphalt AAB undergoes due to aging. Prior to aging, asphalt AAB has two distinctive phases which are distributed randomly in nearly equivalent percentages. Phase 1 appears to disperse Phase 2, and the creep measurements support this notion. After aging, the same two phases appear to still perform a similar role in terms of material behavior, but the shape, size and distribution of these two phases have changed significantly, not to mention, an additional phase, Phase 3, now exists as an apparent sub-phase of Phase 2. Furthermore, Phase 2 appears to have dispersed during the aging process. Prior to aging, the approximate distribution of Phases 1 and 2 was nearly equivalent at 52 percent and 48 percent, respectively. The approximate distribution of Phases 1, 2 and 3 after aging was

20 percent, 70 percent and 10 percent, respectively. Not only have the phase distributions of the original two phases changed, but the material stiffness of each phase has also increased significantly, which demonstrates that not only do individual phase microstructures and distributions change with age but also the distinct properties of each phase. The material stiffness of Phase 3 demonstrates very similar behavior to that of Phase 2 after aging, which indicates that these two phases possess dissimilar structures but similar material properties. It is also observed that Phase 2, prior to aging, has a very similar response to constant load as Phase 1, after aging. The approximate increase in stiffness due to aging of Phase 1 and Phase 2 was 27 percent and 14 percent, respectively.

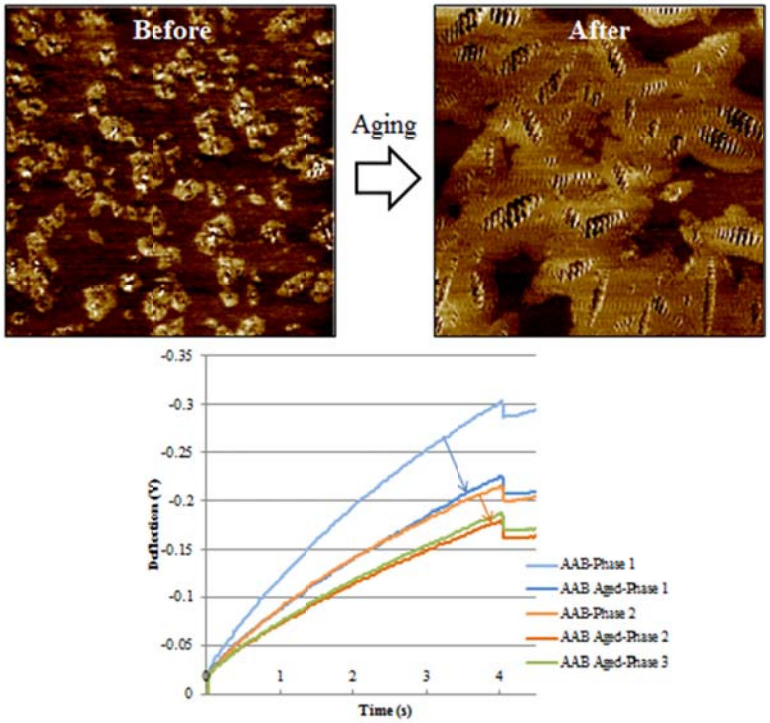

Figure 4.28. Effects of aging on asphalt AAB.

Figure 4.29 demonstrates a similarly extensive microstructural transformation of asphalt AAD due to long-term aging. Prior to aging, asphalt AAD had two distinctive phases which were distributed randomly. Phase 1 was predominant and appeared to disperse Phase 2, and creep measurements support this notion. After aging, Phase 1 still appears to be the dispersing phase, but dispersion of Phase 2 caused the structure to completely transform and become seemingly organized into a repeating pattern surrounding by newly formed Phase 3. As observed in asphalt AAB, Phase 3 of asphalt AAD is assumed to be a sub-phase of Phase 2, since the phase is only evident directly within Phase 2. The approximate distribution of Phases 1 and 2 prior to aging was 85 percent and 15 percent, respectively. The approximate distribution of Phases 1, 2 and 3 after aging was 17 percent, 45 percent and 38 percent, respectively. Not only have the phase distributions of the original two phases changed but the material stiffness of each phase has also considerably increased, which reiterates the occurrence of individual phase property change with age, in addition to individual phase microstructure and distribution change. Unlike observations of aged asphalt AAB, Phase 3 of aged asphalt AAD exhibits unique stiffness behavior from Phases 1 and 2, which indicates that Phase 3 is a distinctive phase with dissimilar structure and material behavior. It is also observed that all aged asphalt phases possess higher stiffness than corresponding original phase stiffness's. The approximate increase in stiffness due to aging of Phase 1 and Phase 2 was 58 percent and 57 percent, respectively.

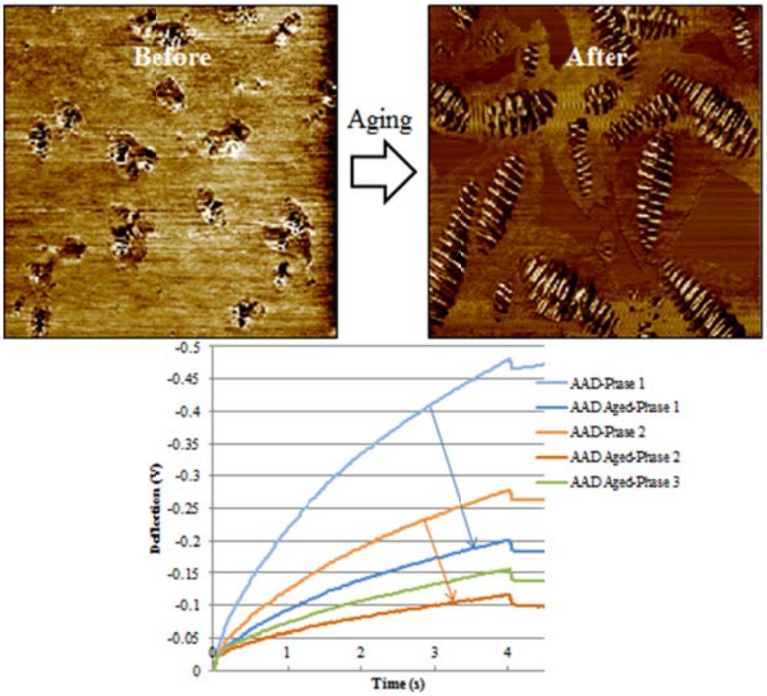

Figure 4.29. Effects of aging on asphalt AAD.

Despite many efforts to obtain a phase image depicting noticeably different microstructures for asphalt ABD, including the application of various AFM imaging techniques and processing of images ranging from 5 to 100 µm, no such image was acquired. Instead, a phase image depicting varying shades of color was obtained, in which phases were identified and force measurements were taken based on the observed differences. Prior to aging, asphalt ABD had two distinctive phases which were distributed randomly in nearly equivalent percentages. Although the original two phases still exist after aging, a subtle increase in distribution of Phase 2 and subsequent decrease in Phase 1 was evident. An important observation that was not apparent from the phase images of asphalt ABD was the occurrence of molecular clustering due to aging. An indication of molecular clustering was offered by a substantial increase in S_a and S_q due to aging. Prior to aging, the approximate distribution of Phases 1 and 2 was 48 percent and 52 percent, respectively. After aging, the approximate distribution of Phases 1 and 2 was 41 percent and 59 percent, respectively. Figure 4.30 demonstrates the distribution and change in stiffness of each phase before and after aging. It is apparent that aging of asphalt ABD resulted in a change in phase distribution and a considerable increase in stiffness of both phases; however, it is also observed that the variance between each phase stiffness is more apparent prior to aging. The approximate increases in stiffness due to aging of Phase 1 and Phase 2 were 63 percent and 56 percent, respectively.

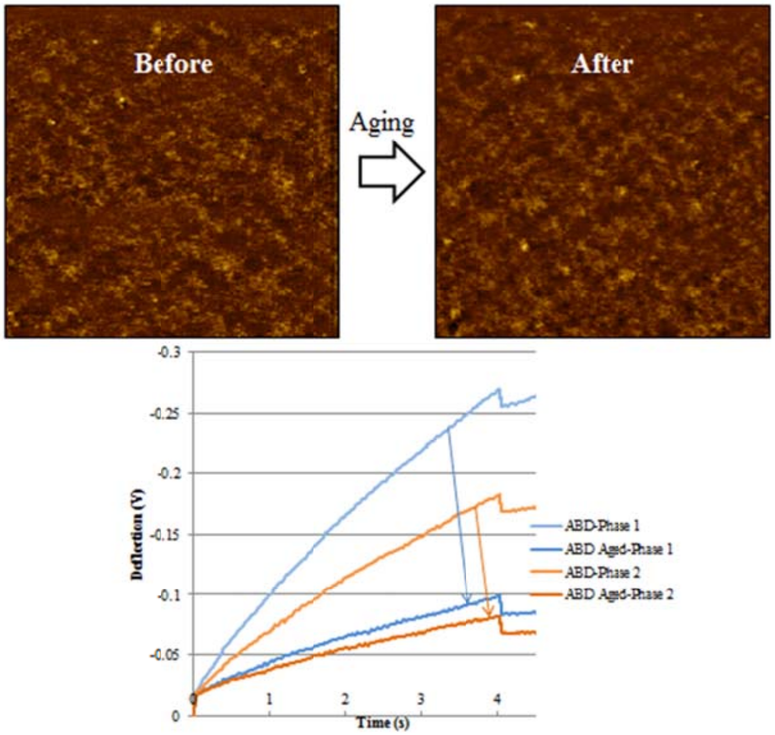

Figure 4.30. Effects of aging on asphalt ABD.

The differences in micromechanical behavior of asphalts AAB, AAD and ABD due to aging have been clearly presented. Further comparison and observation of microstructural change induced by aging is presented in Figure 4.31. As shown, asphalt AAD has the least overall stiffness prior to aging and a notably lower stiffness than asphalt AAB, based on individual phase creep measurements; however, asphalt AAB exhibits the least overall stiffness after aging. This indicates that aging has a more profound effect on the microstructural change of asphalt AAD than asphalt AAB. The effects of aging on asphalt ABD are also significantly greater than that of asphalt AAB. In fact, aging appears to have a similar overall impact on asphalts AAD and ABD in terms of stiffness change of individual phases.

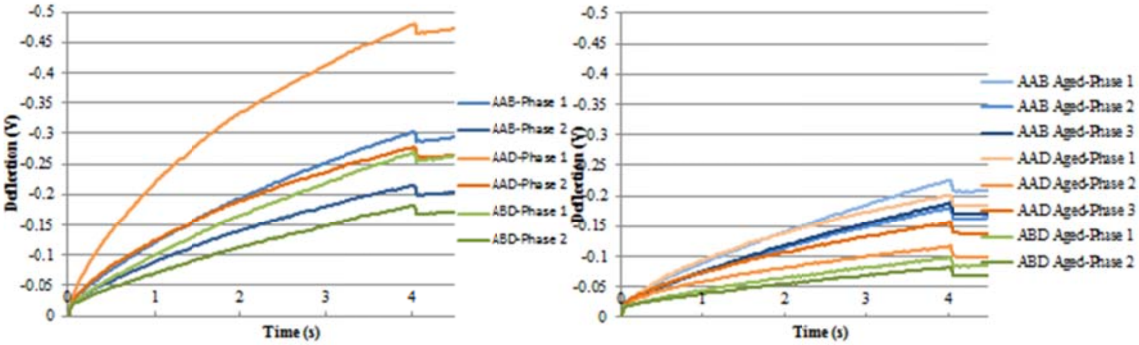

Figure 4.31. Creep measurement comparison of aged and unaged asphalts AAB, AAD and ABD.

As shown in Table 4.2, a combination each asphalt phase distribution, maximum deflection under constant load and respective standard deviation of measurements were used to generate a macro-scale prediction of asphalt deflection representing the microstructural behavior of PDM-identified micro-phases in each asphalt. The possible percentage error of the prediction was also included and calculated based on the standard deviation of measurements from the mean measurement. Also shown in Table 4.2 are viscoelastic material properties, complex shear modulus (G*) and penetration index (PI), as determined by SHRP and documented by the SHRP MRL in 1993. G* values for asphalt ABD were not available for the original and PAV aged asphalt, so these values were estimated, strictly for comparison purposes, based on correlations from the available TFOT-aged G* value for asphalt ABD. The purpose of the comparisons between stiffness values obtained during this experiment and the SHRP MRL-documented viscoelastic material properties was to validate the force measurements collected during this study and to observe any common trends or correlations between the two data sets. Although microstructural creep measurements provide fundamentally different information regarding viscoelastic behavior than G* and PI data, overall stiffness correlations and common trends between these different data sets were still needed to validate the creep measurements. The macro-scale predictions of the creep measurements collected during this study should show a common trend compared to G*, which represents a material's total resistance to deformation when repeatedly sheared and PI, which describes material stiffness based on depth of needle penetration under constant load. Explicitly, a decrease in maximum creep deflection should generally correspond to a decrease in PI and increase in G*. For asphalts AAB, AAD and ABD the maximum deflection correlated well with the PI values. In each case, a higher PI value corresponded to a higher maximum deflection value. Positive correlations were also consistently observed between G* and the micro-deflection data; e.g., increase in G* due to aging was accompanied by a decrease in micro-deflection for each asphalt.

These correlations provide validation that the force measurements collected during the experiment yielded reasonable results.

Table 4.2. Comparison of Phase Distribution and Deflection Data.

Asphalt	**Phase Distribution and Maximum Creep Deflection/ Deflection St. Dev.**									**Macro-scale Prediction**			**SHRP data comparison**	
	Phase 1			Phase 2			Phase 3			Defl. (V)	S. D. (V)	± Error (%)	G* (Pa)	Pen (0.1 mm)
	%	Defl. (V)	S. D. (V)	%	Defl. (V)	S. D. (V)	%	Defl. (V)	S. D. (V)					
AAB	52	0.30	0.07	48	0.21	0.06	NA	NA	NA	**0.26**	0.06	25	2,486	98
AAB-aged	20	0.22	0.07	70	0.18	0.05	10	0.19	0.08	**0.19**	0.06	30	8,888	NA
AAD	85	0.48	0.11	15	0.28	0.17	NA	NA	NA	**0.45**	0.12	26	3,148	135
AAD-aged	17	0.20	0.03	45	0.12	0.05	38	0.16	0.03	**0.15**	0.04	26	11,319	NA
ABD	48	0.27	0.02	52	0.18	0.05	NA	NA	NA	**0.22**	0.04	16	5,197*	47
ABD-aged	41	0.10	0.004	59	0.08	0.01	NA	NA	NA	**0.09**	0.01	10	18,662*	NA

*estimated for comparison purposed based on similar correlations

5. CONCLUSIONS, RECOMMENDATIONS AND FUTURE WORK

This section summarizes the main findings of this experiment, provides links to related studies and offers recommendations for the continued investigation of asphalt microstructure using AFM.

5.1 DETAILED CONCLUSIONS AND RECOMMENDATIONS

Based on the results obtained from phase images, profile extractions, three-dimensional phase depictions, surface texture statistical analysis, graphical phase distribution and creep measurements presented in the previous section, two conclusive observations are readily apparent: all PDM-identified microstructures observed in this experiment demonstrate different material behavior under constant load, and the effects of long-term aging profoundly impact not only the material behavior of these microstructures but also the shape, size and distribution of each asphalt microstructure. The primary findings in this study include:

- Prior to aging, asphalts AAB, AAD and ABD each consisted of two distinctive PDM-identified phases. After aging, asphalt ABD consisted of two phases; whereas, asphalts AAB and AAD each consisted of three phases.
- Long-term aging clearly induces microstructural change in asphalt. The form and extent of these changes, however, were different for each asphalt studied. The three types of microstructural changes observed during this study were: dispersion of phase, clustering of phase and materialization of phase. Dispersion

of phase was observed in Phase 2 of asphalts AAB and AAD. Clustering of phase was observed in Phase 2 of asphalt ABD, and materialization of phase was observed within Phase 2 of asphalts AAB and AAD by the appearance of a new sub-phase within Phase 2, which was identified as Phase 3 or “bee” structure.

- Long-term aging not only induces changes in phase structure and distribution, but also in the distinct properties of each phase. In other words, age-induced stiffness increase is not exclusively due to the presence of greater percentages of higher stiffness components after aging. Although results indicate that this is partially the case, distinctive changes in the properties of each phase also occur and contribute greatly to the higher stiffness, which strongly indicates polar interactions within each PDM-identified phase.
- Aging resulted in a stable reduction in percentage of Phase 1 and subsequent steady increase in percentage of Phase 2. Furthermore, Phase 1 exhibited the lowest stiffness, and Phase 2 showed the highest stiffness for each asphalt before and after aging.
- Prior to aging, apparent dispersed phases exhibited stiffness’s ranging from 42 to 50 percent greater than the apparent dispersing phase; after aging, more variability was observed amongst the values as dispersed phase stiffness’s varied from 22 to 67 percent greater than the dispersing phases. Phase 3, which was only observed directly within Phase 2 after aging, exhibited an intermediary stiffness ranging from 6 to 45 percent less than the encircling Phase 2.

- Aging has a more profound effect on the microstructural behavior of asphalts AAD and ABD than on asphalt AAB.
- Creep measurements taken from each PDM-identified phase indicated heterogeneous domains in asphalt with clearly different mechanical properties. The data collected from these measurements indicated the same overall trend as the viscoelastic material properties determined by SHRP and documented by the SHRP MRL in 1993, which provides validity and reliability to the data collected during this study.

The use of PDM in this study has aided in successfully validating asphalt as a non-homogeneous mixture of different microstructural entities. Since PDM is not only sensitive to geometric or topographic differences but also to differences in mechanical properties, the separation of these regions by PDM provided a necessary boundary for further investigation of dissimilarities in micromechanical behavior amongst different phases. As emphasized by Masson, et al (2005), microstructural behavior of organic material such as asphalt, is governed by the size, flexibility and mutual interactions of asphalt compounds by means of hydrogen, ionic or polar bonds; therefore, it is important to establish relationships between the asphalt phases identified in this study and asphalt microstructural characteristics such as chemical composition and polarity.

The micellar structural model of asphalt, in which asphaltenes are stabilized by polar aromatics in a sea of naphthene aromatics and saturated compounds (Pfeiffer and Saal, 1940), is often referenced by researchers (Loeber et al., 1996; Pauli et al., 2001 and Masson et al., 2005) as a basis for comparison to various PDM-detected phases in asphalt, despite the fact that correlations between the micellar model and field performance have never been made. The individual contributions of the micellar model components include: asphaltenes as viscosity or stiffness-building components, polar aromatics as ductility-providing components, napthene aromatics as softening components that change with age and saturates as liquids that change very little with age (Roberts, et. al 1996). Inconsistencies between these expected contributions of components and field performance are revealed by observing data previously presented in Tables 3.1 and 3.2. As shown, asphalt ABD has the lowest asphaltenes content and highest saturates content but yields the highest stiffness of the three asphalts, which contradicts one of the fundamental concepts of the model. Furthermore, asphalt AAD has the highest asphaltenes content and exhibits the least stiffness of the three asphalts. Such evidence of inconsistencies in the relationship between the model and performance indicates that the model is unreliable in predicting asphalt microstructural material behavior, and hence, should not be referenced as a basis for comparison to the micromechanical behavior of various PDM-identified phases.

Early AFM researchers, Loeber et al. (1996) and Pauli et al. (2001), attributed the “bee” structures to asphaltenes, which suggests that these structures act as stiffness and viscosity-building components of asphalt; however, creep measurements obtained during this study indicate that the “bee” structures play somewhat of a different role. In fact, these structures consistently exhibited a lower stiffness, or weak zone, within the surrounding phase. Masson et al. (2005) established that there is a poor correlation between asphaltenes and the PDM-identified “bee” structures, and as demonstrated, this experiment supports the same hypothesis.

SHRP implemented advances in technology which led to a better understanding of asphalt chemistry through the development of the microstructural model. According to the model, the two fractions, SEC I and SEC II, were isolated from asphalt and were believed to contain mostly “associated molecules” and “solvent molecules,” respectively. Performance-based asphalt tests have shown that increased amounts of SEC I result in increased brittleness, low-temperature cracking and fatigue cracking. Further analysis by SHRP researchers depicted asphalt as a “three-dimensional molecular matrix of highly polar molecules swollen by its more neutral molecules. The three-dimensional nature makes it somewhat elastic, but, with sufficient stress (thermal or mechanical) the weak bonds rearrange and the asphalt experiences permanent strain (Roberts et al 1996).” The preceding description depicted by the SHRP researchers seems applicable and somewhat analogous to the phase images and corresponding force measurements obtained in this study. Based on the notion that the microstructural model is accurate and depicts asphalt as a single-phase system containing many complex molecules of different polarity, it is unlikely that the observed phases have any association with generic fractions depicted in the micellar model. Considering that molecules commonly used as building blocks for organic synthesis typically range in size from a few Å to a few dozen Å, and the individual phases depicted in this experiment typically range from 1 to 10 μm, it is likely that the each phase is composed of thousands of molecules. Assuming that this is the case, it is also unlikely that each phase is composed of only polar or non-polar molecules that are depicted in the microstructural model, but rather a unique combination of polar and non-polar molecules within each phase that results in substantially different material behavior of each phase. As indicated by the results and analysis previously detailed, Phase 2 consistently exhibits the highest stiffness before and after aging, and Phase 1 consistently displays the lowest stiffness. This trend specifies the presence of more highly polar molecules in Phase 2 than Phase 1, based on the microstructural model of asphalt. According to phase images, Phase 1 only exhibits minor change during the aging process, but an obvious stiffness increase indicates significant change in chemical composition caused by molecular associations within the phase. Although Phase 2 appears to disperse during aging, which would contradict the notion of clustering or molecular associations of highly polar molecules within the phase, the resulting Phase 2 structure is likely the product of molecular organizations into a more stable, although dispersed, arrangement within the phase. Based on the force measurements and associated patterns of abruptly shifting high and low elevations that are characteristic of Phase 3, there is a strong indication that these regions are “weak zones” somehow formed during the molecular bonding and organization within Phase 2. The Phase 3 regions are thought to be regions that are highly susceptible to permanent strain or perhaps regions that have already endured permanent strain. This hypothesis indicates that while asphalt becomes more stable during aging through molecular organizations, unavoidable weak zones are also formed that are highly susceptible to permanent strain and, thus, induce pavement distress. This hypothesis furthermore offers a possible visual explanation to the findings of the SHRP researchers in which higher percentages of SEC I resulted in increased brittleness and cracking.

Considering the many hindrances that can occur during an AFM experiment of this magnitude, such as preventing 1 μm thin films of asphalt from becoming contaminated or rapidly oxidizing prior to testing, minimizing the artifacts that commonly plague AFM, or repeating roughly 140 force measurements in different phases of a highly adhesive material with a single AFM cantilever probe; the comparisons made between the measurements obtained during this experiment and the data documented in the SHRP MRL showed exceptional correlations. Certain variability in force measurements was revealed for many of the asphalt phases, but such variability was expected, especially considering the highly variable nature of asphalt. The primary goal of this study was to distinguish between the material behavior of different asphalt micro-phases, and aside from a few unforeseen challenges, such as piezo creep and thermal drift issues that resulted in an inability to measure micro-phase recovery, the overall execution of the research objective was extremely successful.

By using PDM to isolate different asphalt microstructures and SM to collect relative creep measurements from each of these locations, data were collected which corroborated expected mechanical differences of each asphalt phase. Furthermore, the collected data provided the foundation for valuable comparisons to existing models and documented asphalt data. The fact that microstructural and material behavior fluctuations occur as asphalt ages is not a new idea, but the extent to which these changes occur is still widely misunderstood. This research has offered new perspective into the impact of aging on the microstructural behavior of asphalt. Further study of the magnitude of aging effects on the micro-properties of asphalt should be pursued. Additional research is also clearly needed to validate the “weak zone” hypothesis, but continued investigation in this area could lead to a focused effort to minimize or reduce the formation of these “weak zones” and successively result in longer-lasting HMA pavements.

5.2 LIMITATIONS OF STUDY

This study was an initiation phase that was necessary to determine whether significant variations in mechanical properties existed within different micro-phases in asphalt, but as pointed out by Cuenot et al. (2004), such an experiment should incorporate more advanced stages that are necessary to determine the influence of surface mechanics on measured micromechanical properties. Furthermore, the findings from this study should ultimately be implemented into a new or existing model to improve its accuracy in predicting HMA performance by reducing some of the assumptions required to build such a model.

5.3 FUTURE WORK

Although some advances in technology will be required to continue studying asphalt microstructure using AFM, the following related topics are recommended for further research: the effects of short-term aging, moisture and temperature on micromechanical behavior; the investigation of micromechanical behavior of asphalts not included in this study; the application of alternate cantilever tips, such as spherical tips, to collect force measurements and the measurement of micro-phase recovery in various asphalt phases.

REFERENCES

AASHTO R 28 and ASTM D6521-08 (1996-2010): “Accelerated Aging of Asphalt Binder Using a Pressurized Aging Vessel (PAV).” *Book of Standards*, 4(3), ASTM International, West Conshohocken, PA.

AASHTO T 240 and ASTM D 2872 (1996-2010). “Effect of Heat and Air on a Moving Film of Asphalt (Rolling Thin-Film Oven Test).” *Book of Standards*, 4(3), ASTM International, West Conshohocken, PA.

Agilent Technologies, Inc. (2007). *Agilent 5400 Scanning Probe Microscope User’s Guide*, Palo Alto, California.

Burnham, N.A., and Colton R.J. (1989). “Measuring the Nanomechanical Properties and Surface Forces of Materials Using an Atomic Force Microscope.” *Journal of Vacuum Science and Technology*, 7(4), 2906-2913.

Burnham, N.A., Dominguez, D.D., Mowery, R.L., and Colton, R.J. (1990). “Probing the Surface Forces of Monolayer Films with an Atomic-Force Microscope.” *Physical Review Letters*, 64(16), 1931-1934.

Butt, H-J., Capella, B., and Kappl, M. (2005). “Force Measurements with the Atomic Force Microscope: Technique, Interpretation and Applications.” *Surface Science Reports*, 59, 1-152.

Costa, K.D., and Yin, F.C.P. (1999). “Analysis of Indentation: Implications for Measuring Mechanical Properties with Atomic Force Microscopy.” *Journal of Biomechanical Engineering*, 121, 462-471.

Cuenot, S., Frétigny, C., Demoustier-Champagne, S., and Nysten, B. (2004). "Surface Tension Effect on the Mechanical Properties of Nanomaterials Measured by Atomic Force Microscopy." *Physical Review*, 69, 165410-1-165410-5.

Eaton, P.J., Graham, P., Smith, J.R., Smart, J.D., Nevell, T.G., and Tsibouklis, J. (2000). "Mapping the Surface Heterogeneity of a Polar Blend: An Adhesion-Force-Distribution Study Using the Atomic Force Microscope." *Langmuir*, 16, 7887-7890.

Howland, R., and Benatar, L. (2000). "A Practical Guide to Scanning Probe Microscopy" *Thermoscopes,* 1-87.

Huang, S-C., Turner, T.F., Pauli, A.T., Miknis, F.P., Branthaver, J.F., and Robertson, R.E. (2005). "Evaluation of Different Techniques for Adhesive Properties of Asphalt-Filler Systems at Interfacial Region." *Journal of ASTM International*, 2(5), 1-15.

Jäger, A., Lackner, R., Eisenmenger-Sittner, C., Blab, R. (2004). "Identification of Microstructural Components of Bitumen by Mean of Atomic Force Microscopy (AFM)." *Proceedings of the Applied Mathematics and Mechanics Society*, 4, 400-401.

Jones, D.R., and Kennedy T.W. (1992) "The Asphalt Model: Results of the SHRP Asphalt Research Program" Center for Transportation Research, The University of Texas at Austin, Austin TX.

Loeber, L., Sutton, O., Morel, J., Valleton, J.-M., and Muller, G. (1996). "New Direct Observations of Asphalts and Asphalt Binders by Scanning Electron Microscopy and Atomic Force Microscopy." *J. Microsc*. 182, 32–39.

Magonov, S.N., and Reneker, D.H. (1997). "Characterization of Polymer Surfaces with Atomic Force Microscopy." *Annual Review of Material Science*, 27, 175-222.

Masson, J-F., Leblond, V., and Margeson, J. (2005). "Bitumen Morphologies by Phase-detection Atomic Force Microscopy." *Journal of Microscopy*, 221(1), 17-29.

Masson, J-F., Leblond, V., and Margeson, J. (2007). "Low-temperature Bitumen Stiffness and Viscous Paraffinic Nano- and Micro-Domains by Cryogenic AFM and PDM." *Journal of Microscopy*, 227(3), 191-202.

Mortazavi, M., and Moulthrop, J.S. (1993). "The SHRP Materials Reference Library" *The Strategic Highway Research Program*, SHRP-A-646, Washington, D.C.

Oyekunle, L.O. (2006). "Certain Relationships between Chemical Composition and Properties of Petroleum Asphalts from Different Origin." *Oil & Gas Science and Technology*, 61(3), 433-441.

Pauli, A.T., Branthaver, J.F., Robertson, R.E., and Grimes, W. (2001). "Atomic Force Microscopy Investigation of SHRP Asphalts." *Symposium on Heavy Oil and Resid Compatibility and Stability*, pp. 110–114. Petroleum Chemistry Division, American Chemical Society, San Diego, California.

Pfeiffer, J.P.H., and Saal, R.N.J. (1940). "Asphaltic Bitumen as a Colloid System." *J. Phys. Chem*. 44, 139–149.

Raghavan, D., VanLandingham, M., Gu, X., and Nguyen, T. (2000). "Characterization of Heterogeneous Regions in Polymer Systems Using Tapping Mode and Force Mode Atomic Force Microscopy." *Langmuir*, 16, 9448-9459.

West, P., Starostina, N. (2009) "AFM Image Artifacts." *Lot-Oriel Gruppe Europa*, 58, 1-8. www.lot-oriel.com/site/site_down/pn_artifacts_deen.pdf.

Winkler, R.G., Spatz, J.P., Sheiko, S., Möller, M., Reineker, P., and Marti, O. (1996). "Imaging Material Properties by Resonant Tapping-Force Microscopy: A Model Investigation." *Physical Review*, 54(12), 8908-8912.

VITA

Robert Grover Allen received his Bachelor of Science degree in civil engineering from Louisiana Tech University in February 2006. Upon graduation, he worked as a project engineer at Applied Research Associates (ARA) from March 2006 to August 2009. He entered graduate school at Texas A&M University in September 2009 and received his Master of Science degree in civil engineering in December 2010. While earning his master's degree, he worked as a research assistant at Texas Transportation Institute (TTI) in College Station, Texas.

He can be reached at the email address: grvallen@yahoo.com or at the mailing address shown below.

Texas Transportation Institute
601C CE/TTI Building, TAMU 3135
Texas A&M University System
College Station, TX 77843-3135